SANDIA REPORT
SAND2017-4461
Unlimited Release
Printed April, 2017

Radiation-MHD simulations for the development of a spark discharge channel

John H. J. Niederhaus, Roy E. Jorgenson, Larry K. Warne, and Kenneth C. Chen

Prepared by
Sandia National Laboratories
Albuquerque, New Mexico 87185 and Livermore, California 94550

Sandia National Laboratories is a multi-mission laboratory managed and operated by Sandia Corporation, a wholly owned subsidiary of Lockheed Martin Corporation, for the U.S. Department of Energy's National Nuclear Security Administration under contract DE-AC04-94AL85000.

Approved for public release; further dissemination unlimited.

Sandia National Laboratories

Issued by Sandia National Laboratories, operated for the United States Department of Energy by Sandia Corporation.

NOTICE: This report was prepared as an account of work sponsored by an agency of the United States Government. Neither the United States Government, nor any agency thereof, nor any of their employees, nor any of their contractors, subcontractors, or their employees, make any warranty, express or implied, or assume any legal liability or responsibility for the accuracy, completeness, or usefulness of any information, apparatus, product, or process disclosed, or represent that its use would not infringe privately owned rights. Reference herein to any specific commercial product, process, or service by trade name, trademark, manufacturer, or otherwise, does not necessarily constitute or imply its endorsement, recommendation, or favoring by the United States Government, any agency thereof, or any of their contractors or subcontractors. The views and opinions expressed herein do not necessarily state or reflect those of the United States Government, any agency thereof, or any of their contractors.

Printed in the United States of America. This report has been reproduced directly from the best available copy.

Available to DOE and DOE contractors from
U.S. Department of Energy
Office of Scientific and Technical Information
P.O. Box 62
Oak Ridge, TN 37831

Telephone: (865) 576-8401
Facsimile: (865) 576-5728
E-Mail: reports@osti.gov
Online ordering: http://www.osti.gov/scitech

Available to the public from
U.S. Department of Commerce
National Technical Information Service
5301 Shawnee Rd
Alexandria, VA 22312

Telephone: (800) 553-6847
Facsimile: (703) 605-6900
E-Mail: orders@ntis.gov
Online order: http://www.ntis.gov/search

SAND2017-4461
Unlimited Release
Printed April, 2017

Radiation-MHD simulations for the development of a spark discharge channel

John H. J. Niederhaus
Multiphysics Applications

Roy E. Jorgenson and Larry K. Warne
Electromagnetic Theory

Kenneth C. Chen
Nuclear Safety Assessment

Sandia National Laboratories
P.O. Box 5800
Albuquerque, New Mexico 87185-MS1323

Abstract

The growth of a cylindrical spark discharge channel in water and Lexan is studied using a series of one-dimensional simulations with the finite-element radiation-magnetohydrodynamics code ALEGRA. Computed solutions are analyzed in order to characterize the rate of growth and dynamics of the spark channels during the rising-current phase of the drive pulse. The current ramp rate is varied between 0.2 and 3.0 kA/ns, and values of the mechanical coupling coefficient K_p are extracted for each case. The simulations predict spark channel expansion velocities primarily in the range of 2000 to 3500 m/s, channel pressures primarily in the range 10-40 GPa, and K_p values primarily between 1.1 and 1.4. When Lexan is preheated, slightly larger expansion velocities and smaller K_p values are predicted, but the overall behavior is unchanged.

CONTENTS

1. INTRODUCTION 9

2. MECHANICS OF SPARK CHANNEL EXPANSION 11

3. ALEGRA SIMULATIONS 13
   3.1. Initial Condition 13
   3.2. Boundary Conditions 13
   3.3. Computational Mesh 14
   3.4. Material Models 15

4. WATER AND LEXAN SPARK CHANNEL SIMULATIONS 17
   4.1. Water and Lexan Solution Profiles 17
   4.2. Channel Mechanical Analysis 20

5. SPARK CHANNEL SENSITIVITY STUDIES 25
   5.1 Preheated material 25
   5.2 Current ramp rate 29
   5.3 Mesh resolution 31

6. CONCLUSIONS 33

7. REFERENCES 35

APPENDIX A: TATB SPARK CHANNEL SIMULATIONS 37
   A.1. Approximations for TATB material configuration 37
   A.2. Dense Lexan and TATB solution profiles 39
   A.3. Extent-of-reaction profiles for active TATB 43
   A.4. Channel mechanical analysis for dense Lexan 45
   A.5. Channel preheat analysis for dense Lexan and TATB 46
   A.6. Large ramp rates for dense Lexan 51
   A.7. Mesh resolution study 52
   A.8. Dense Lexan and TATB summary 53

APPENDIX B: REFERENCE SIMULATION DATA 55
   B.1. Density profiles 55
   B.2. Temperature profiles 56
   B.3. Pressure profiles 56
   B.4. Mean channel pressure histories 57
   B.5. Mean channel radius histories 58
   B.6. Coupling coefficient histories 58

APPENDIX C: EXAMPLE INPUT FILE (LEXAN) 59

DISTRIBUTION 64

FIGURES

Figure 1: Layout of ALEGRA spark channel simulations (not to scale), showing the orientation of the current density vector just after initialization. 13
Figure 2: Time snapshots of density profiles computed by ALEGRA for 0.2 and 0.8 kA/ns. 17
Figure 3: Time snapshots of electrical conductivity profiles computed by ALEGRA for 0.2 and 0.8 kA/ns. 18
Figure 4: Time snapshots of temperature profiles computed by ALEGRA for the 0.2 and 0.8 kA/ns cases. 19
Figure 5: Time snapshots of pressure profiles computed by ALEGRA for the 0.2 and 0.8 kA/ns cases. 20
Figure 6: Channel radius $a(t)$ for water at 0.2 and 0.8 kA/ns. 21
Figure 7: Channel expansion rate da/dt for water at 0.2 and 0.8 kA/ns. 21
Figure 8: Mean channel pressure $p(t)$ for water at 0.2 and 0.8 kA/ns. 21
Figure 9: Channel mechanical coupling coefficient for water at 0.2 and 0.8 kA/ns. 21
Figure 10: Channel radius $a(t)$ for Lexan at 0.2 and 0.8 kA/ns. 23
Figure 11: Channel expansion rate da/dt for Lexan at 0.2 and 0.8 kA/ns. 23
Figure 12: Mean channel pressure $p(t)$ for Lexan at 0.2 and 0.8 kA/ns. 23
Figure 13: Mechanical coupling coefficient Kp for Lexan at 0.2 and 0.8 kA/ns. 23
Figure 14: Mechanical coupling coefficient Kp for water and Lexan at 0.4 kA/ns. 24
Figure 15: Time snapshots of density profiles computed by ALEGRA for Lexan at 0.2 and 0.8 kA/ns, at baseline (left) and with an initial preheated temperature of 250˚C (right). 25
Figure 16: Time snapshots of temperature profiles computed by ALEGRA for Lexan at 0.2 and 0.8 kA/ns, at baseline (left) and with an initial preheated temperature of 250˚C (right). 26
Figure 17: Channel expansion history for Lexan at 0.2 and 0.8 kA/ns, at baseline (left) and with an initial preheated temperature of 250˚C (right). 27
Figure 18: Histories of the mechanical coupling coefficient Kp for Lexan at 0.2 and 0.8 kA/ns, at baseline (left) and with an initial preheated temperature of 250˚C (right). 28
Figure 19: Time snapshots of pressure profiles in Lexan for high current ramp rates. 29
Figure 20: Mean channel pressure $p(t)$ in Lexan at high current ramp rates. 30
Figure 21: Ramp-rate dependence of Lexan channel expansion velocity vch and Kp. 30
Figure 22: Density (left) and pressure (right) profiles at t = 100 ns in water at 0.8 kA/ns, for coarse and fine meshes (dx = 200, 100, 50, 25 nm). 31
Figure 23: Zoomed-in views of the shock front in density (left) and pressure (right) profiles at t = 100 ns in water at 0.8 kA/ns, for coarse and fine meshes (dx = 200, 100, 50, 25 nm). 32
Figure 24: Resolution study for (left) channel expansion velocity and (right) coupling coefficient for water at several ramp rates. 32
Figure 25: Time snapshots of dense Lexan and TATB density profiles computed by ALEGRA for the 0.2 and 0.8 kA/ns cases. 40
Figure 26: Time snapshots of dense Lexan and TATB electrical conductivity profiles computed by ALEGRA for the 0.2 and 0.8 kA/ns cases. 41
Figure 27: Time snapshots of dense Lexan and TATB temperature profiles computed by ALEGRA for the 0.2 and 0.8 kA/ns cases. 42
Figure 28: Time snapshots of dense Lexan and TATB pressure profiles computed by ALEGRA for the 0.2 and 0.8 kA/ns cases. 43
Figure 29: Profiles of the extent of reaction for TATB for a range of current ramp rates. 44

Figure 30: Channel radius $a(t)$ for dense Lexan at 0.4 and 0.8 kA/ns..... 45
Figure 31: Channel mechanical coupling coefficient Kp for dense Lexan at 0.4 and 0.8 kA/ns. 45
Figure 32: Time snapshots of density computed by ALEGRA for the 0.8 kA/ns case at baseline (left) and with an initial preheated temperature of 250˚C (right)..... 47
Figure 33: Time snapshots of temperature computed by ALEGRA for the 0.8 kA/ns case at baseline (left) and with an initial preheated temperature of 250˚C (right)..... 48
Figure 34: Channel expansion history (left) and mechanical coupling coefficient Kp (right) for dense Lexan for the 0.8 kA/ns case with an initial preheated temperature of 250˚C..... 48
Figure 35: Profiles of the extent of reaction for TATB for a range of current ramp rates an initial preheated temperature of 250˚C..... 50
Figure 36: Time snapshots of pressure profiles in dense Lexan for high current ramp rates..... 51
Figure 37: Mean channel pressure $p(t)$ in dense Lexan at high current ramp rates..... 52
Figure 38: Density (left) and pressure (right) profiles at t = 100 ns in water at 0.8 kA/ns, for coarse and fine meshes (dx = 200, 100, 50, 25 nm)..... 53
Figure 39: Profiles of TATB extent of reaction at t = 100 ns at (left) 0.4 kA/ns and (right) 0.6 kA/ns, for coarse and fine meshes (dx = 200, 100, 50, 25 nm)..... 53
Figure 40: Density profiles for water (above) and Lexan (below)..... 55
Figure 41: Temperature profiles for water (above) and Lexan (below)..... 56
Figure 42: Pressure profiles for water (above) and Lexan (below)..... 56
Figure 43: Mean channel pressure histories for water (above) and Lexan (below)..... 57
Figure 44: Average channel pressure at t = 60 ns as a function of current ramp rate..... 57
Figure 45: Channel radius histories for water (above) and Lexan (below)..... 58
Figure 46: Coupling coefficient (K_p) histories for water (above) and Lexan (below)..... 58

TABLES

Table 1: Material properties and computational material models used in ALEGRA simulations. 15
Table 2: Channel expansion rates (linear fit) and mean coupling coefficient values for water and Lexan..... 24
Table 3: Channel expansion rates (linear fit) and mean coupling coefficient values for Lexan at baseline, and with an initial preheated temperature of 250˚C..... 28
Table 4: Channel expansion rates (linear fit) and mean coupling coefficient values for Lexan at high current ramp rates..... 30
Table 5: Material properties and computational material models used in ALEGRA simulations for TATB. Information for water and Lexan from Table 1 is duplicated here for reference.. 38
Table 6: Channel expansion rates (linear fit) and mean coupling coefficient values for dense Lexan..... 46
Table 7: Channel expansion rates (linear fit) and mean coupling coefficient values for dense Lexan at baseline and with an initial preheated temperature of 250˚C..... 49
Table 8: Average channel pressure in water and Lexan sampled at t = 60 ns for high current ramp rates..... 57

NOMENCLATURE

DOE	Department of Energy
EOS	Equation of state
HEDP	High-energy-density physics
HVRB	History variable reactive burn
LMD	Lee-More-Desjarlais
MHD	Magnetohydrodynamics
SNL	Sandia National Laboratories
TATB	Triamino-trinitrobenzene
a	Channel radius
dx	Mesh resolution
K_p	Mechanical coupling coefficient
$\bar{p}$	Mean channel pressure
ϕ	Extent of reaction
s_r	Density scaling factor for EOS model
s_c	Electrical conductivity scaling factor
v_{ch}	Mean (linear-fit) channel expansion velocity

1. INTRODUCTION

Spark channels are of interest because of the consequences of high-voltage breakdown and discharge events in engineering applications. These events can cause intense and destructive local heating, and can generate strong shock waves that propagate into the surrounding material, leading to potentially critical mechanical loads. When the medium is an energetic material, the consequences can be even more severe.

A spark channel forms when a breakdown event rapidly energizes a column of otherwise electrically insulating material connecting electrodes with a high potential difference. This column of material suddenly becomes much more conductive than the surrounding material. It forms a relatively low-resistance pathway, leading to discharge with very high electric current densities. Depending on the inductance of the system, the current may rise very quickly, initiating overwhelming localized Joule heating that forms a column of high-pressure, heated material. This column must expand into the surrounding low-pressure medium, forming an expanding shock wave. The continued flow of current and Joule heating in this system, together with radiative heat transport and shock dynamics make the subsequent behavior complex.

Here we study a simple representation of this system, where the spark channel is a cylinder and the system can be studied in one spatial dimension (r). The system is studied using numerical modeling with the radiation-magnetohydrodynamics (MHD) code ALEGRA [1]. The high-energy-density physics (HEDP) module in ALEGRA has been used previously in studies of this type, with good results [2,3]. Discharges in water and Lexan (polycarbonate) are studied here, and for these two materials, twelve current ramp rates are studied, between 0.2 and 3.0 kA/ns.

The remainder of this report includes a discussion of the mechanics of spark channel expansion and a description of the ALEGRA code and the setup of these simulations, followed by a discussion and analysis of simulation material models and results. Properties of the simulations for water and Lexan are examined, including solution profiles, channel expansion characteristics, and extracted K_p values. Finally, we discuss a set of simulations where the materials are assumed to be preheated to 250˚C prior to the spark channel formation. Together these form a simple overview that may be useful in understanding and predicting how a spark may affect materials in these situations.

In Appendix A, an additional series of simulations is discussed, for the insensitive high explosive TATB (triamino-trinitrobenzene), over a similar range of ramp rates. Certain approximations in the material properties are required to obtain meaningful radiation-MHD modeling results for TATB, since its electrical conductivity and some regions of its equation of state (EOS) are not well characterized. Channel expansion characteristics and extracted K_p values are shown and discussed for these approximations in the appendix.

2. MECHANICS OF SPARK CHANNEL EXPANSION

Localization of current density and Joule heating is a characteristic property of spark channels. Therefore, it is typically easy to locate the boundary or "wall" of the hot, current-carrying channel, and characterize its motion over time. Locating this boundary allows a simple mechanical analysis of spark channel behavior. As the channel expands, it radiates heat to the surrounding medium, and drives an expanding shock wave. The transfer of momentum and energy from the channel to the surrounding medium, while the channel expands into the medium, is important for determining what effect the original breakdown event will have on the larger medium.

In the symmetric case we have chosen, the channel wall and expanding shock wave are both cylindrical. A simple model for the mechanical coupling between the expanding channel emerges from a momentum balance across the channel wall. In this model, the rate of channel expansion is related to the pressure in the channel and the exterior density through a dimensionless mechanical coupling coefficient K_p. In the work of Warne et al (2005) [2], this quantity is defined by the relationship

$$K_p = \frac{\bar{p}}{\rho}\left(\frac{da}{dt}\right)^{-2} \tag{1}$$

where a is the channel radius, $\bar{p}$ is the mean pressure in the channel, and ρ is the initial density of the channel material. Smaller values of K_p indicate a smaller mean channel pressure is needed to achieve the same rate of momentum transfer to the medium via shock expansion.

3. ALEGRA SIMULATIONS

The finite-element multiphysics code ALEGRA [1] is used here. The HEDP (high-energy-density physics) module of the code is used, so that radiative heat transport can be included. ALEGRA uses a finite-element representation with explicit time integration for an equation of motion that includes the full internal stress tensor and the Maxwell stress arising from magnetohydrodynamics (MHD). The timestep is constrained by the local sound speed and magnetosonic speeds. The local energy update on each step includes contributions from radiation, Joule heating, and thermal conduction, in addition to the mechanical work. Each material includes models for the equation of state, the opacity, and the electrical and thermal conductivity, which span thermodynamic conditions ranging from ambient to fully ionized plasma conditions. Discretizations and finite-element degrees of freedom are chosen in ALEGRA which fit into a "DeRham" diagram, ensuring that the magnetic induction is exactly divergence free by construction ($\nabla \cdot \vec{B} = 0$). These are called "mimetic" or "compatible" discretizations. Implicit linear solvers are coupled into the system via operator splitting, to handle the elliptic problems associated with transient magnetic diffusion, thermal conduction, and radiation diffusion.

3.1. Initial Condition

Since ALEGRA is constrained by the MHD approximation, the physics involved in dielectric breakdown itself cannot be simulated directly. Instead, the simulation must begin at a point when sufficient heating has occurred along the breakdown path to make it a bulk-neutral, conductive plasma column, but the channel has not yet begun to expand radially. Therefore, the initial condition is taken to be a cylinder of material at ambient density (unexpanded, $\rho_c = \rho_0$) with a temperature T_c = 1 eV = 11,604.5 K. An equation of state model is evaluated to obtain the pressure under these conditions: $p_c = p(\rho_c, T_c)$. Exterior to the channel, the medium is at ambient density, pressure, and temperature. The initial radius a_0 of the channel is taken to be 10 μm (there is a rapid progression to a radius of hundreds of microns), corresponding with similar previous work [3]. The exterior extends to R = 1 mm. The geometry is shown schematically in Figure 1.

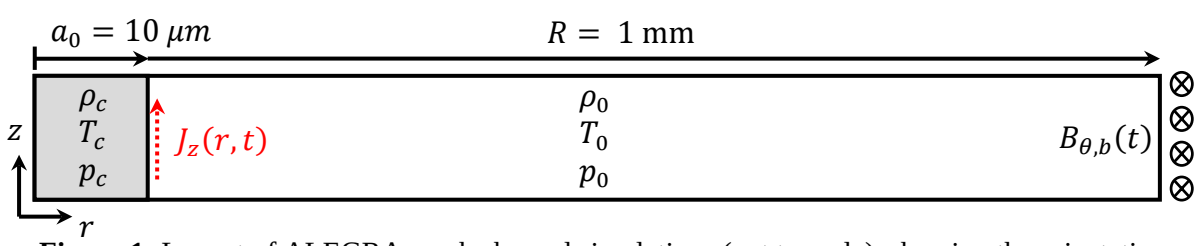

Figure 1: Layout of ALEGRA spark channel simulations (not to scale), showing the orientation of the current density vector just after initialization.

3.2. Boundary Conditions

After initialization, an axial current flow with steadily increasing magnitude current is fed into the system. The current ramp rate $\dot{I}$ is fixed: that is, inductive feedback to the driving circuit is ignored and the driver is assumed to be an infinite charge reservoir. Current is fed to the system by imposing an azimuthal tangent magnetic induction $B_{\theta,b}$ at the outer radial boundary of the domain:

$$B_{\theta,b}(t) = \frac{\mu_0 I(t)}{2\pi R} = \frac{\mu_0 \dot{I} t}{2\pi R} \tag{2}$$

Under the thermodynamic conditions imposed at time zero, the channel material is conducting, and all of the material exterior to the channel is strongly insulating. Therefore, the transient magnetics formulation in ALEGRA will force a total current I to flow axially along the conducting cylindrical channel, in correspondence with the imposed field, as depicted in Figure 1. The local current density J_z will be dependent on the evolution of the system and the distribution of electrical conductivity.

The simulations are configured on a two-dimensional Lagrangian mesh, shown conceptually in Figure 1. In effect, however, the simulations are one-dimensional (1D). Only a single row of elements in r comprises the mesh, and the natural boundary condition of zero tangential electric field is imposed at the $\pm z$ boundaries. This constrains the magnetic field vector to point in the $\pm\theta$ direction only, and the current density and electric field to point in the $\pm z$ direction only. In order to enforce cylindrical symmetry, the code solves the axisymmetric (r-z) formulation of the equations, recast with the quantity rB_θ as the unknown for transient magnetics (for accuracy), with $rB_\theta = 0$ imposed at $r = 0$.

Thus, the simulations represent the ideal scenario of a perfectly cylindrical 10-μm-radius discharge channel carrying current during the rising side of a current pulse. As time proceeds, the channel material undergoes tremendous Joule heating, with a local volumetric heating rate of $J_z^2(r,t)/\sigma(r,t)$, where $\sigma(r,t)$ is the local electrical conductivity. The channel expands due to the pressure difference relative to the exterior, and the expansion is sustained by continued deposition of internal energy via Joule heating.

At the very high temperatures reached in the channel, thermal conduction and radiative heat transfer become important, and are therefore included in the simulations via operator splitting, with additional linear solves required on each timestep. This allows some energy to be lost from the channel and/or transmitted to the nearby surrounding material. The thermal conduction model is based on Fourier's law with variable thermal conductivity $\kappa(r,t)$, using insulating boundary conditions (zero heat flux) at the $\pm z$ and $r = 0$ boundaries. The radiation model is single-group diffusion with variable scattering and absorption opacities defined for each material. Reflective boundary conditions are used at the $\pm z$ and $r = 0$ boundaries, and a vacuum boundary condition at the $+r$ boundary.

3.3. Computational Mesh

The quasi-1D Lagrangian mesh for these simulations is comprised of 100 initially evenly-spaced elements for $r \leq a_0$) – therefore the initial mesh spacing in the channel is 0.1 μm. The exterior region is filled with elements linearly biased in radial size from 0.1 μm at $r = a_0$ to 0.425 μm at $r = R$. This yields approximately 3,900 total elements in the mesh. In the z-direction, the element size is set to 0.5 μm.

Some testing was done using an Eulerian mesh, but for some of the TATB cases considered here, these simulations typically require the use of *ad hoc* limiters on forces or Joule heating to prevent runaway excursions in dynamic and thermodynamic properties late in time. Meshes at coarser resolution also result in anomalous artifacts in the thermodynamic profiles for some cases.

3.4. Material Models

For these radiation-MHD simulations, the following material properties are required for the full range of temperatures and densities encountered in the system: equation of state (EOS), electrical and thermal conductivity, and opacity for radiative heat transfer. Because of the large pressures and short timescales involved in the system, fluid viscosity and material strength are both neglected. Some material properties, and the selected model types used here for each of these categories is shown in Table 1.

Table 1: Material properties and computational material models used in ALEGRA simulations.

	Water	**Lexan**
Ambient density (kg/m^3)	1000	1185
Ambient electrical conductivity (S/m)	4.80×10^{-8}	4.33×10^{-8}
Electrical conductivity (S/m), T = 1 eV	1.44×10^{5}	2.14×10^{4}
Electrical / thermal conductivity model	LMD customized	LMD "Lexan"
EOS model	Sesame 7150	ANEOS Sesame 7751
Opacity model	Tabular "water"	Tabular "CH"

For water and Lexan, EOS and electrical/thermal conductivity models are readily available in the material data provided with the ALEGRA code, and from previous work. For the water EOS model, Sesame table 7150 is used, which is the standard recommended water model used in ALEGRA and includes the liquid-vapor phase change, ionization, and dissociation products in chemical equilibrium [5]. For the Lexan EOS model, an ANEOS solid-liquid-gas model with ionization is used [6], tabulated as Sesame table 7751, which has been used extensively in shock-MHD simulations with ALEGRA. The ambient density in these models is shown in Table 1.

The electrical and thermal conductivity for Lexan and water is provided by the Lee-More-Desjarlais (LMD) model [7], which has been employed successfully in numerous MHD and radiation-MHD modeling studies with ALEGRA. For water, the LMD model is parameterized using the same configuration as was used by Warne *et al*. in 2005 [2]. For Lexan, the standard LMD parameterization for ALEGRA is obtained by using the "material = 'lexan'" keyword. The electrical conductivity for these models at ambient conditions and at ambient pressure with a temperature of 1 eV is shown in Table 1. Radiative-heat-transfer opacity for water and Lexan is obtained using ALEGRA's Tabular Opacity model. The "H2O" parameterization is used for water, and the "CH" parameterization for Lexan.

4. WATER AND LEXAN SPARK CHANNEL SIMULATIONS

ALEGRA simulations in one dimension are conducted for water and Lexan using the conditions and material configurations described above, for several current ramp rates: $\dot{I} = 0.2$, 0.3, 0.4, 0.5, 0.6, 0.8, 1.0, and 1.2 kA/ns. (Additional ramp rates up to 3.0 kA/ns are also examined below in Section 5.2.) In all simulations, the driving current rises from zero and increases linearly for the duration of the simulation, which is 100 ns.

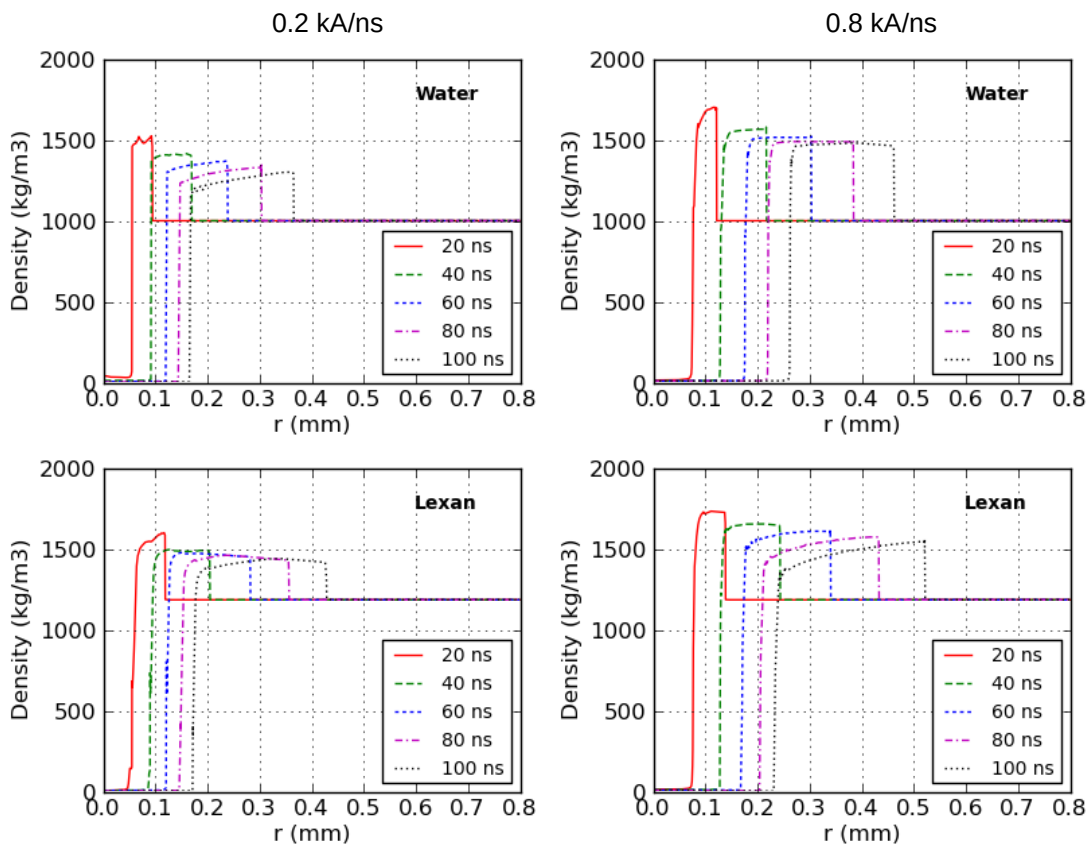

Figure 2: Time snapshots of density profiles computed by ALEGRA for 0.2 and 0.8 kA/ns.

4.1. Water and Lexan Solution Profiles

Representative solution profiles in certain variables are included here in Figures 2 - 5, showing the system evolution through t = 100 ns for selected current ramp rates $\dot{I} = 0.2$, 0.8 kA/ns. Profiles of density appear in Figure 2, and they show characteristic spark channel evolution similar to the results for water shown by Warne et al in 2005 [2]. The spark channel very quickly expands after initialization and drops to very low density. A distinct channel wall forms, where the density jumps abruptly from very small values to shocked values larger than ambient. External to this channel wall, a shock wave propagates outward into undisturbed material, with an amplitude that slowly diminishes as the wave front expands. The peak density and the rate of expansion both increase as the current ramp rate increases.

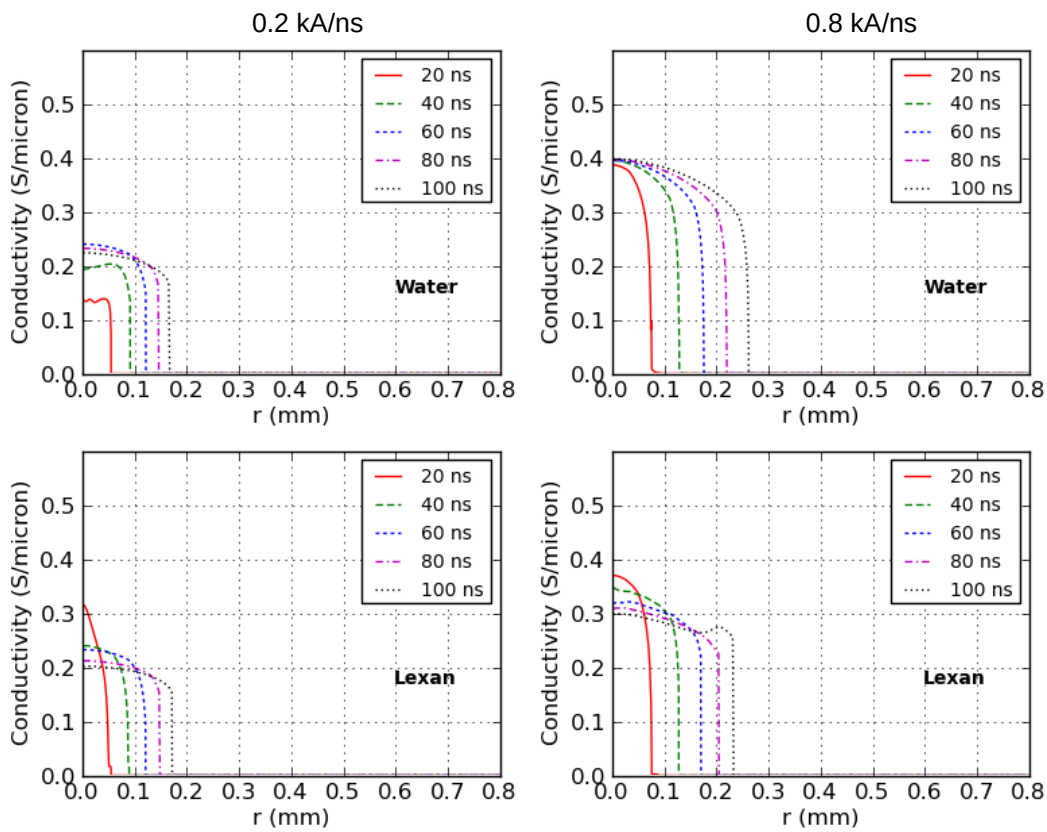

Figure 3: Time snapshots of electrical conductivity profiles computed by ALEGRA for 0.2 and 0.8 kA/ns.

The corresponding profiles in electrical conductivity are shown in Figure 3. The electrical conductivity profiles exhibit a characteristic expanding region of conductive material in the channel. This region is conductive in the sense that it passes current, but its conductivity is only on the order of 10^5 S/m at maximum, several orders of magnitude below that of a conductive metal. Thus, as expected, there are enormous rates of Joule heating in this region, which drive the rapid heating and violent expansion of the channel.

The conductivity drops abruptly back to ambient levels at a radial location that corresponds to the "channel wall" density jump visible in Figure 2. Thus, the conductive region is also the low-density high-temperature region. Since the conductivity defines where the spark current flows, and its location characteristically coincides with the location of the density jump, we use the location of this abrupt jump in conductivity as the definition of the channel radius a. By inspection, we see that the channel expands radially at a rate da/dt on the order of a few km/s at early times (t < 40 ns).

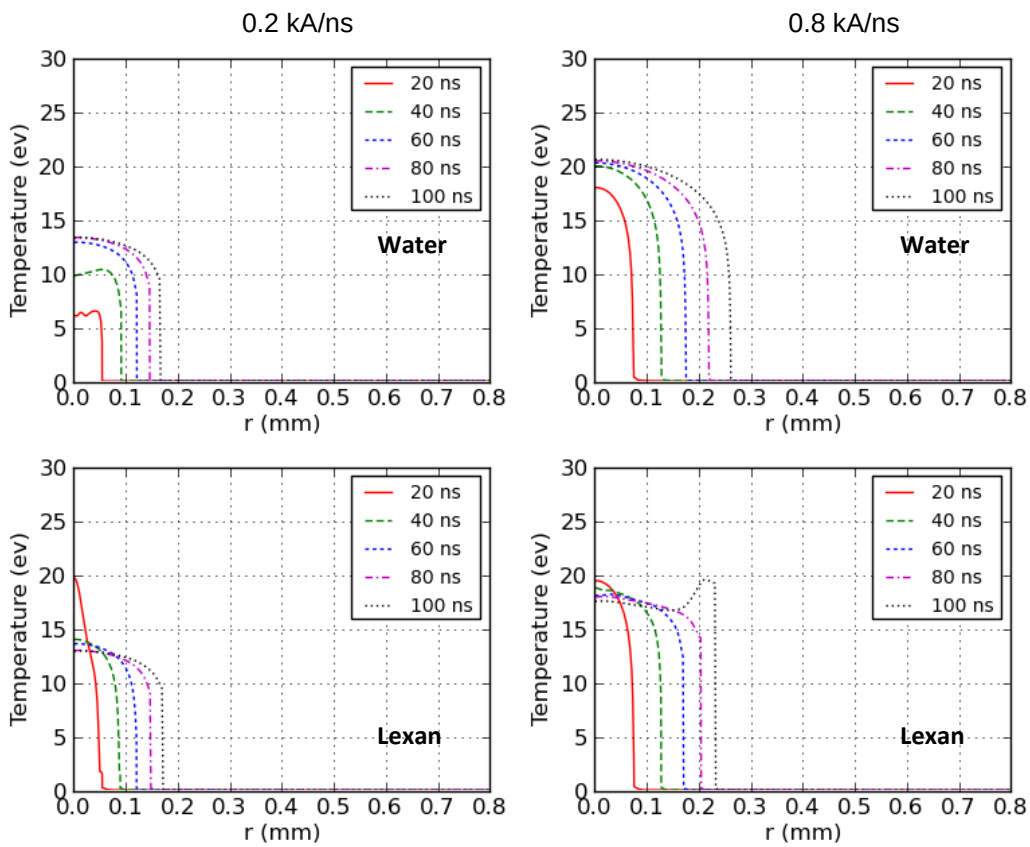

Figure 4: Time snapshots of temperature profiles computed by ALEGRA for the 0.2 and 0.8 kA/ns cases.

Temperature profiles for the representative water and Lexan cases are shown in Figure 4. We see that the temperature in the channel exceeds 10 eV or 100,000 K. The high-temperature region corresponds closely with the conductive region, and the shape of the temperature profile generally corresponds with that of the electrical conductivity profile. Because of the presence of these very large temperatures, thermal conduction and radiative heat transfer must be included in the simulations. For Lexan at 0.8 kA/ns, a strange "horn"-shaped feature appears in the temperature profile near the end of the simulation, visible in Figure 4 as a local maximum at r = 0.2 mm. It also appears less prominently in the electrical conductivity profile seen in Figure 3. This is a temperature excursion that slowly emerges in the Lexan simulations as the ramp rate increases. It is most likely a numerical artifact of the Joule heating calculation in ALEGRA and can be suppressed by activating limiters in the simulation for low densities.

Associated with these very high temperatures are high pressures, which drive the mechanical impulse to the material generated by the spark event. Pressure profiles for these scenarios are shown in Figure 5. The channel mean pressure $\bar{p}$ appears to be on the order of 10 GPa or 100 kbar, with shock wave pressures on the order of a few GPa or 10 kbar. The pressure profile is roughly flat or parabolic within the channel. The local minimum visible in the pressure profiles at 0.8 kA/ns corresponds to the location of the channel wall. The channel pressure and shock pressure both diminish over time, but grow with increasing current ramp rate. As the current ramp rate

increases, a more prominent parabolic shape emerges within the channel, with a pronounced peak at the axis.

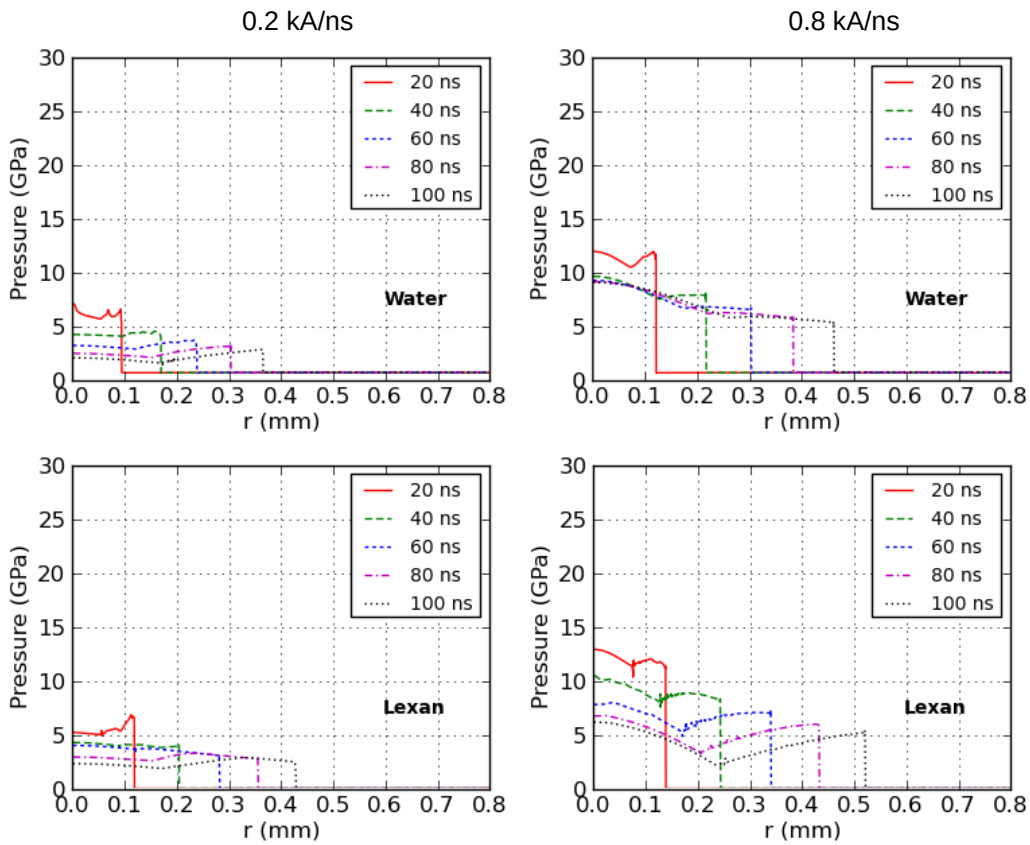

Figure 5: Time snapshots of pressure profiles computed by ALEGRA for the 0.2 and 0.8 kA/ns cases.

4.2. Channel Mechanical Analysis

The mechanical interaction between the spark channel and the medium is analyzed here by measuring the channel expansion rate and its pressure. A value of K_p for each material can then be obtained using the definition in Equation 1. To obtain a rough initial estimate of K_p for water, we may assume an ambient density ρ = 1000 kg/m^3, a channel expansion rate da/dt = 2500 m/s, and a mean channel pressure 10 GPa based on inspection of profiles shown above. This yields a rough estimate of the mechanical coupling coefficient for water as K_p = 1.6.

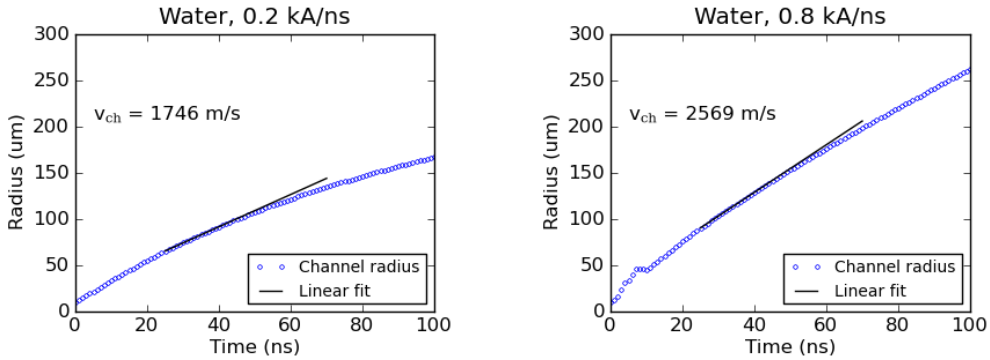

Figure 6: Channel radius $a(t)$ for water at 0.2 and 0.8 kA/ns.

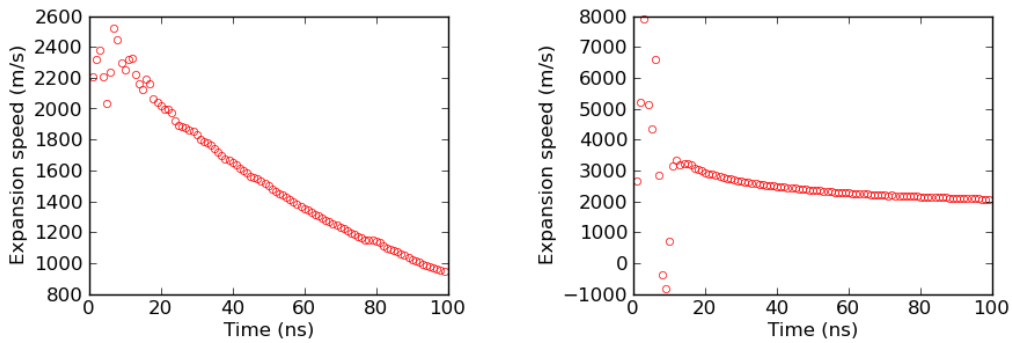

Figure 7: Channel expansion rate da/dt for water at 0.2 and 0.8 kA/ns.

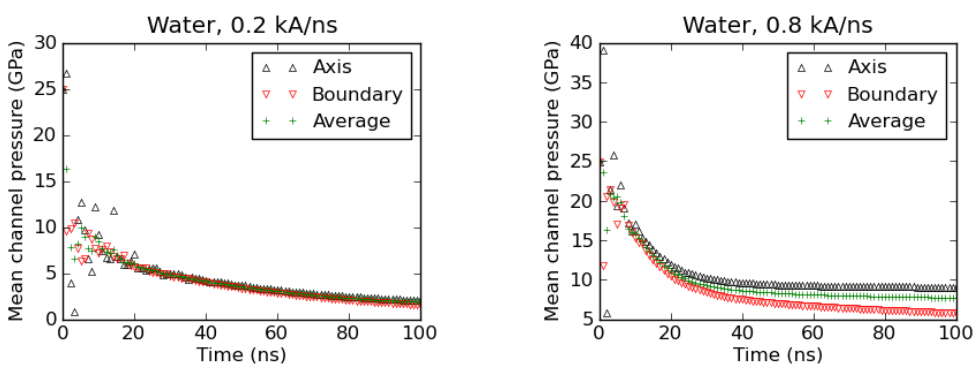

Figure 8: Mean channel pressure $\overline{\boldsymbol{p}}(\boldsymbol{t})$ for water at 0.2 and 0.8 kA/ns.

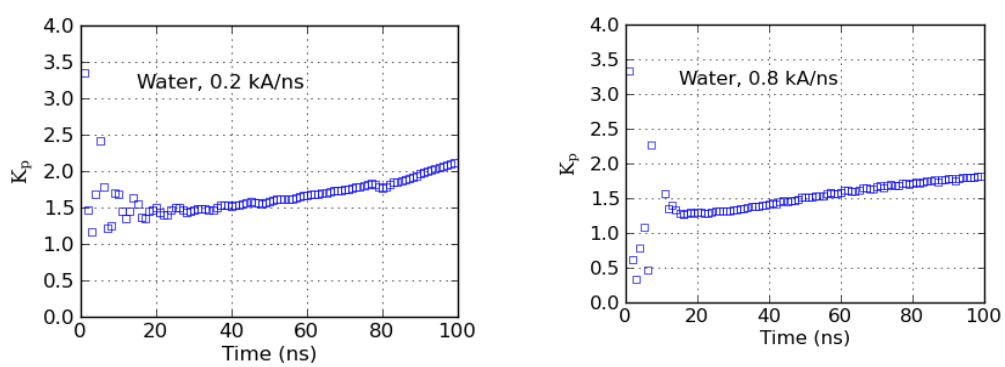

Figure 9: Channel mechanical coupling coefficient for water at 0.2 and 0.8 kA/ns.

In reality, the value of K_p is time-dependent, since the pressure and radial expansion rate both vary over time. They principally diminish, but in the simulations this decline is not necessarily monotonic. To provide a time-varying measurement of K_p here, we use the electrical conductivity jump location as the channel radius $a(t)$, and extract a mean channel pressure $\bar{p}(t)$ by evaluating the simple arithmetic mean of pressure values for $r < a$. That is, the mean pressure is assumed to be the sum of pressures in elements inside the channel wall, divided by the number of those elements – not accounting for the radial variation of element volume.

The sequence of calculated values leading to K_p is shown for the representative water and Lexan cases at 0.2 and 0.8 kA in Figures 6 - 13. In the plots of the channel radius $a(t)$, a linear fit to the data for $25 \leq t \leq 45$ ns is shown (extrapolated to 70 ns). This linear fit provides an estimate v_{ch} for the mean channel expansion velocity in each case, which is also shown in the plots.

A second-order central-difference scheme is used to differentiate the time-dependent channel radius data and obtain an instantaneous expansion speed da/dt, which is plotted in Figures 7 and 11. The time-dependent mean channel pressure is also shown above for these cases, along with the pressure values on axis (r = 0) and at the channel wall ("boundary"). The average channel pressure is used together with the instantaneous expansion velocity and initial ambient material density to obtain a time-dependent history of the coupling coefficient K_p for 0.2 and 0.8 kA/ns, shown in Figures 9 and 13. As an additional piece of information, he time history of K_p for water and Lexan is also shown for 0.4 kA/ns in Figure 14

The overall behavior of the water and Lexan spark systems seen in Figures 6 - 13 is the slow decline of momentum transfer. Although the current continues to climb throughout the simulation, the channel expansion rate slowly diminishes. The pressure inside the channel diminishes initially, then reaches a steadier level after about t = 20 ns.

The final result for K_p shows a high degree of variability, particularly at very early times, resulting from the underlying variability in the extracted expansion velocity and mean pressure. Much of this variability can be ignored, since the expansion velocity estimate depends on the location of the channel wall and the local characteristics of the conductivity profile. The general trend in K_p shows a slow increase in time, and an increase in K_p as the ramp rate increases. That is, the efficiency of the mechanical coupling and momentum transfer between the channel and the exterior medium declines slowly with time and with rising current ramp rate.

A mean value of the coupling coefficient K_p for the period $25 \leq t \leq 45$ ns is computed for all of the current ramp rate cases $0.2 \leq \dot{I} \leq 1.2$ kA/ns. This value, and the linear-fit expansion velocity v_{ch} are both listed for all current ramp rates in Table 2. Overall, for both water and Lexan, the K_p value typically lies in a range between 1.0 and 1.5 for the period between 25 and 45 ns, and mean values of K_p for this period for all ramp rates are 1.435 for water and 1.322 for Lexan.

.

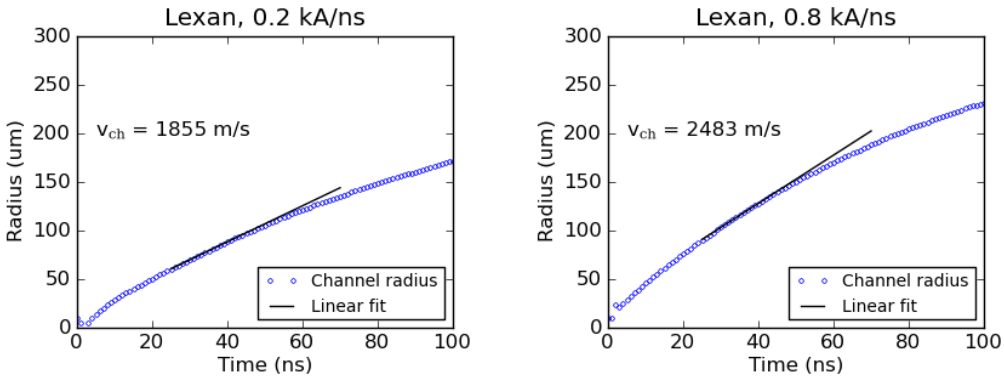

Figure 10: Channel radius $a(t)$ for Lexan at 0.2 and 0.8 kA/ns.

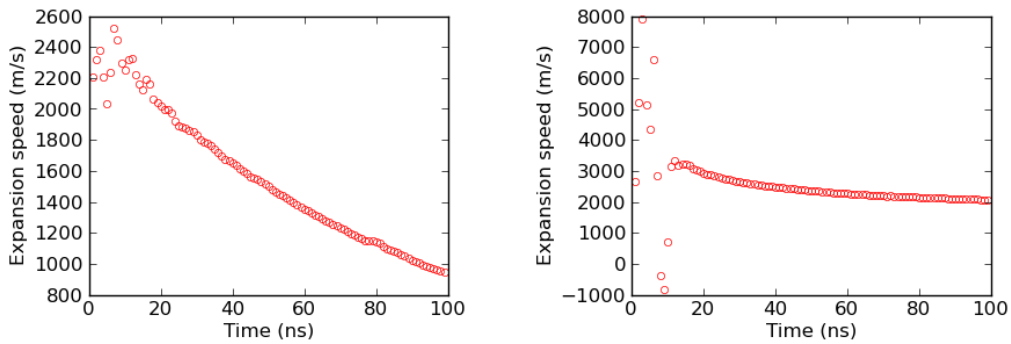

Figure 11: Channel expansion rate da/dt for Lexan at 0.2 and 0.8 kA/ns.

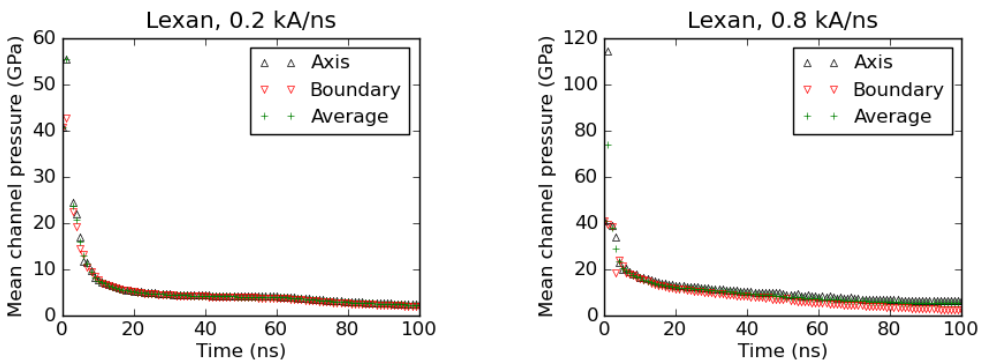

Figure 12: Mean channel pressure $\overline{\boldsymbol{p}}(\boldsymbol{t})$ for Lexan at 0.2 and 0.8 kA/ns.

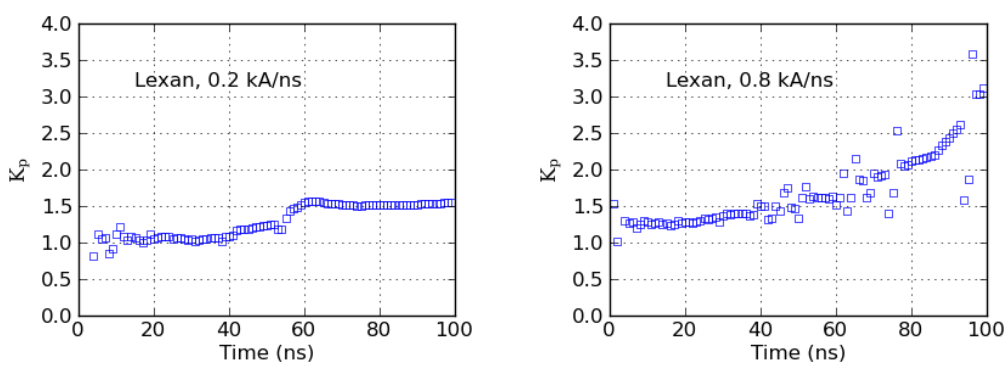

Figure 13: Mechanical coupling coefficient K_p for Lexan at 0.2 and 0.8 kA/ns.

Table 2: Channel expansion rates (linear fit) and mean coupling coefficient values for water and Lexan.

	Water		**Lexan**	
	Expansion velocity v_{ch} (m/s)	Coupling coefficient K_p	Expansion velocity v_{ch} (m/s)	Coupling coefficient K_p
0.2 kA/ns	1746	1.496	1855	1.074
0.3 kA/ns	1919	1.443	2006	1.199
0.4 kA/ns	2049	1.450	2093	1.322
0.5 kA/ns	2197	1.426	2184	1.357
0.6 kA/ns	2329	1.395	2285	1.375
0.8 kA/ns	2569	1.368	2483	1.384
1.0 kA/ns	2670	1.463	2658	1.422
1.2 kA/ns	2796	1.436	2820	1.439
Mean	**-**	**1.435**	**-**	**1.322**

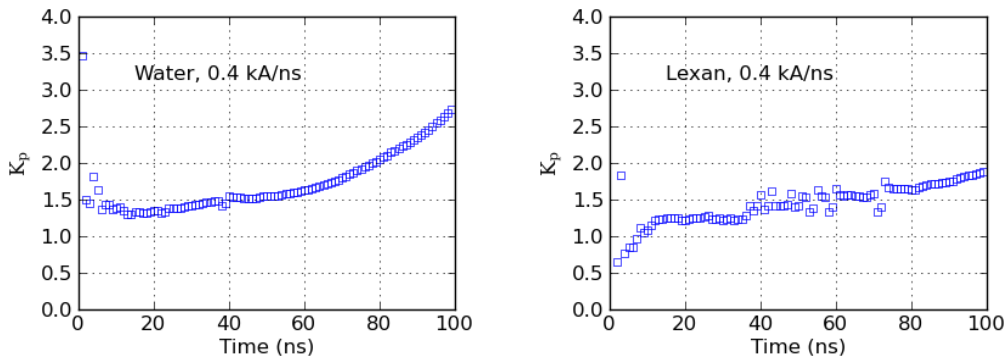

Figure 14: Mechanical coupling coefficient K_p for water and Lexan at 0.4 kA/ns.

5. SPARK CHANNEL SENSITIVITY STUDIES

Using these tests as a baseline, several sensitivity analyses are performed. First, the effect of preheat is examined by applying a high initial temperature to the medium. Second, the effect of higher current ramp rates is examined by extended some cases out to 3.0 kA/ns. Third, the effect of computational mesh resolution is studied by revisiting some of the tests on both coarsened and refined meshes.

5.1 Preheated material

To study the effect of preheat, a series of simulations is conducted – for Lexan only – with an initial temperature of 250˚C in the material exterior to the initial channel. This is done by holding the pressure constant at the ambient value, and reducing the initial density accordingly to match the pressure and imposed initial temperature. In practice, the density is set automatically in ALEGRA using the "initial thermodynamic state" input keyword, together with the imposed initial temperature. This initial, preheated density is 1093 kg/m^3 for Lexan – about 8% lower than the ambient density. Otherwise, the simulations are unchanged from the original series.

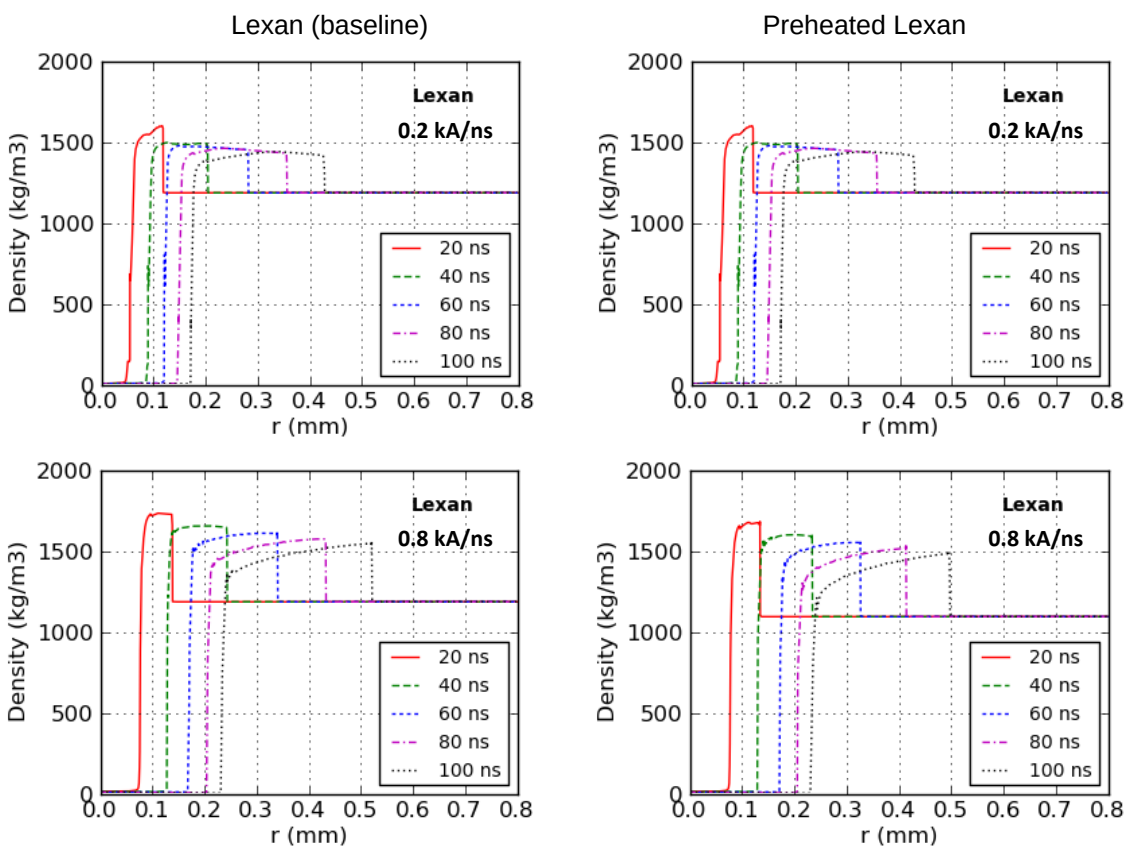

Figure 15: Time snapshots of density profiles computed by ALEGRA for Lexan at 0.2 and 0.8 kA/ns, at baseline (left) and with an initial preheated temperature of 250˚C (right).

Profiles of density and temperature at 0.2 and 0.8 kA/ns are shown for Lexan in Figures 15 and 16. Profile plots from the baseline simulations are duplicated from above for convenient comparison. Water is left out of this study because the water would be in the vapor state at this initial temperature.

With preheat, the characteristic spark channel behavior is seen again, and small changes relative to baseline (ambient temperature and density) are seen. The peak densities are slightly lower with preheat, and the temperatures in the channel are generally slightly higher, with a more pronounced late-time temperature excursion around r = 0.2 mm for 0.8 kA/ns. The spark event therefore seems to produce a slightly more energetic channel with preheat compared to the baseline scenario.

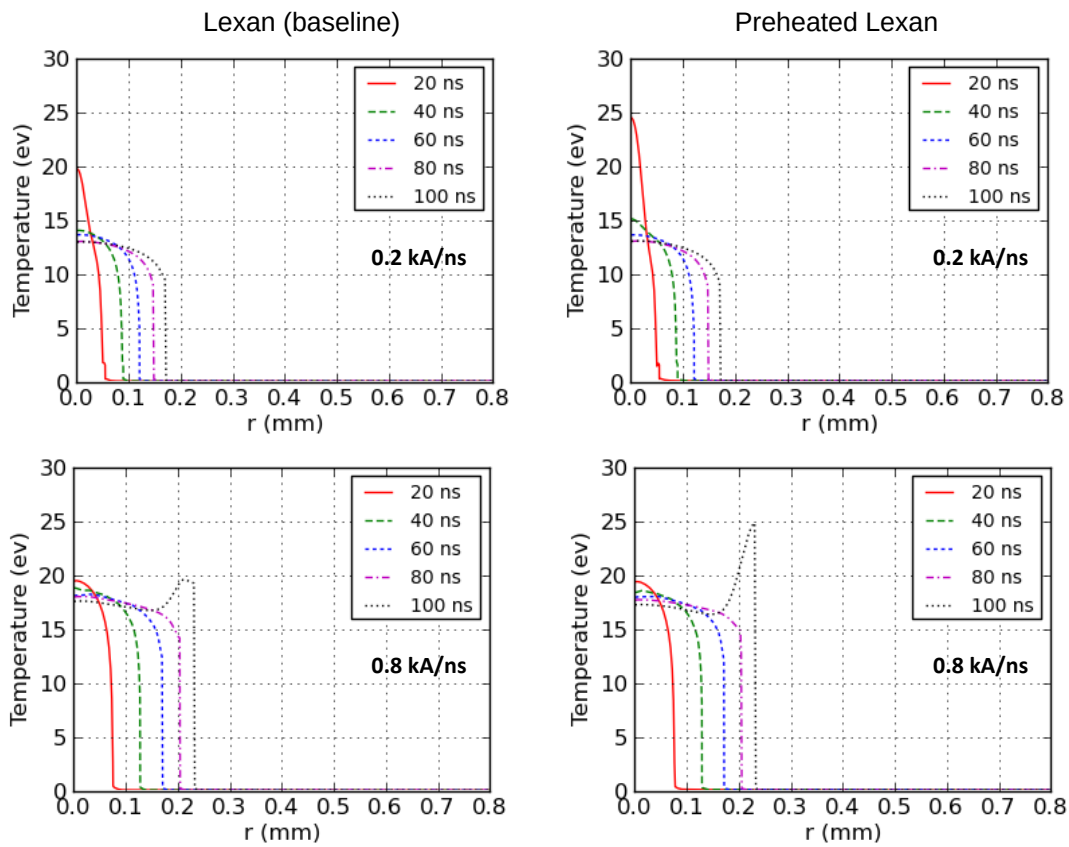

Figure 16: Time snapshots of temperature profiles computed by ALEGRA for Lexan at 0.2 and 0.8 kA/ns, at baseline (left) and with an initial preheated temperature of 250˚C (right).

To quantify this, the same channel radius and K_p analysis is carried here as for the baseline simulations above. The resulting histories of the channel radius and K_p are shown in Figures 17 and 18, and the full set of data is included in Table 3. The baseline results (duplicated from the previous discussion) are included for comparison. We see that the radial channel expansion velocity is indeed slightly higher for the pre-heated cases than for the ambient scenario. Channel pressures and electrical conductivities with pre-heat are not shown here, but the general characteristics of the profiles differ only slightly between the ambient and pre-heated cases.

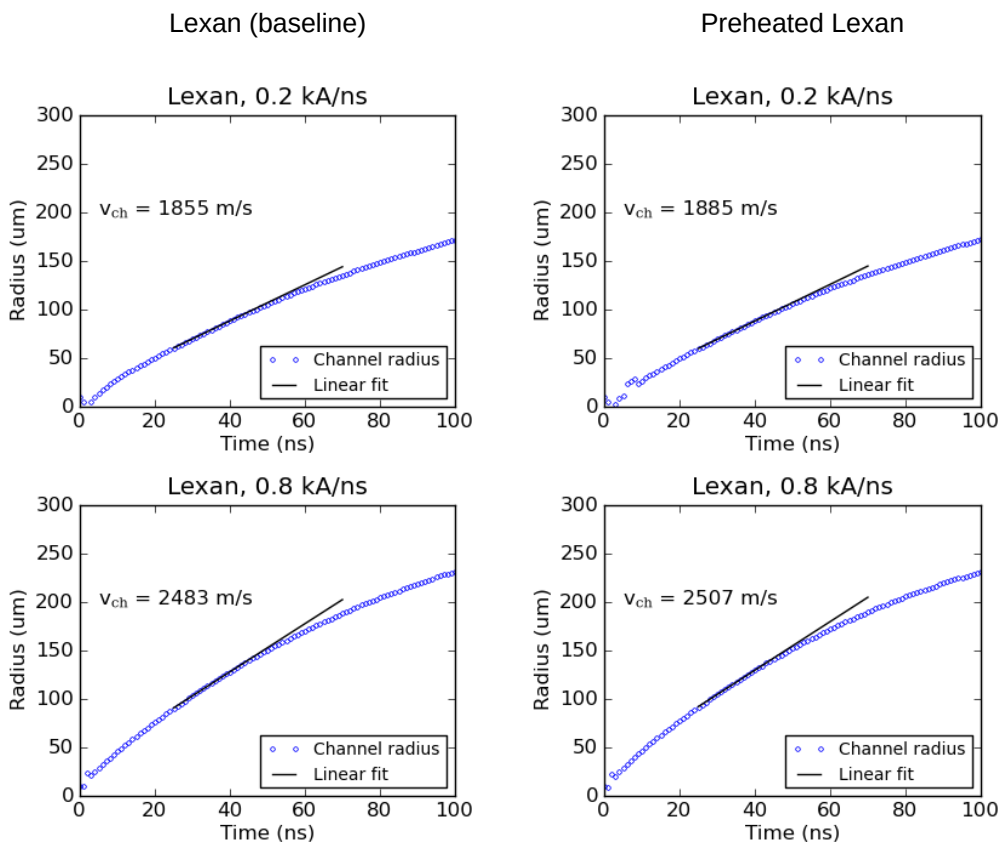

Figure 17: Channel expansion history for Lexan at 0.2 and 0.8 kA/ns, at baseline (left) and with an initial preheated temperature of 250˚C (right).

The slightly larger rates of radial expansion with preheat lead to K_p values that are smaller than the baseline cases for the period $25 \leq t \leq 45$ ns. This can be seen in Figure 18, where the K_p values are generally smaller with preheat compared to baseline at these earlier times, although they are larger at later times. The mean value of the coupling coefficient K_p for the period $25 \leq t \leq 45$ ns is computed for all ramp rates and listed in Table 3, again with the baseline data for comparison. The mean value of K_p over all ramp rates is 1.322 at baseline, and decreases to 1.221 with preheat. Thus, the simulations suggest that a spark event in medium that is already hot (250˚C) is likely to have a slightly lower K_p value and to generate a more quickly expanding spark channel.

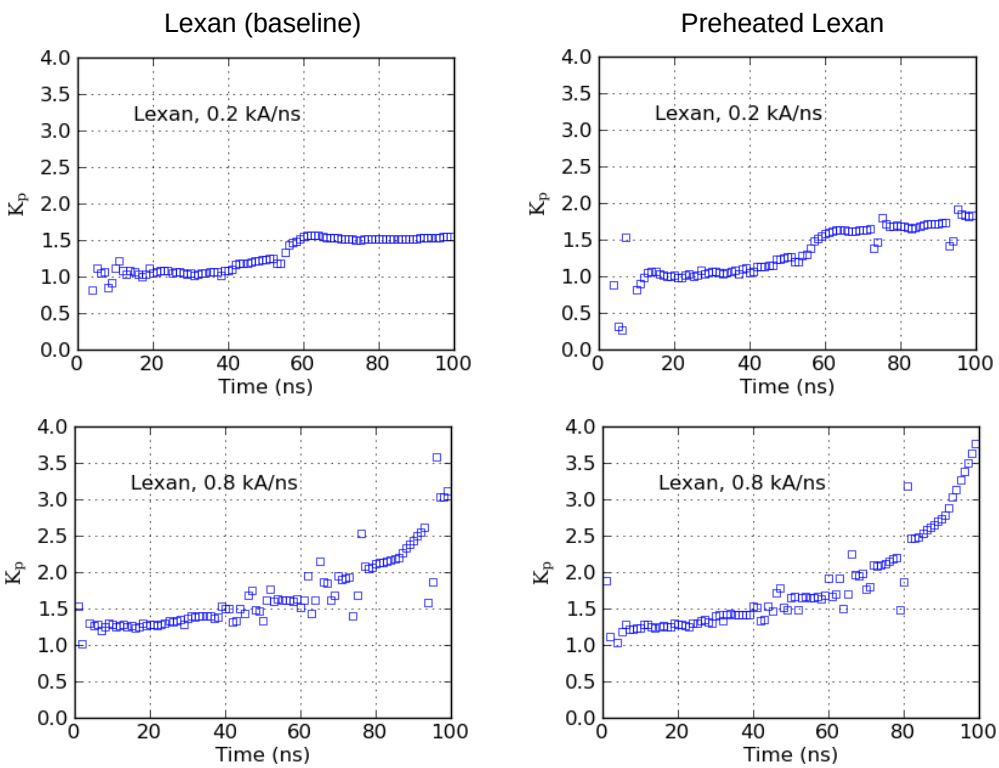

Figure 18: Histories of the mechanical coupling coefficient K_p for Lexan at 0.2 and 0.8 kA/ns, at baseline (left) and with an initial preheated temperature of 250˚C (right).

Table 3: Channel expansion rates (linear fit) and mean coupling coefficient values for Lexan at baseline, and with an initial preheated temperature of 250˚C.

	Lexan (baseline)		**Preheated Lexan**	
	Expansion velocity v_{ch} (m/s)	Coupling coefficient K_p	Expansion velocity v_{ch} (m/s)	Coupling coefficient K_p
0.2 kA/ns	1855	1.074	1885	0.981
0.3 kA/ns	2006	1.199	2023	1.118
0.4 kA/ns	2093	1.322	2138	1.197
0.5 kA/ns	2184	1.357	2222	1.257
0.6 kA/ns	2285	1.375	2313	1.275
0.8 kA/ns	2483	1.384	2507	1.286
1.0 kA/ns	2658	1.422	2674	1.314
1.2 kA/ns	2820	1.439	2830	1.342
Mean	**-**	**1.322**	**-**	**1.221**

5.2 Current ramp rate

To study the effect of higher current ramp rates, the water and Lexan cases are rerun with ramp rates of 1.5, 2, and 3 kA/ns, and all other settings identical to the previous baseline scenarios. Of particular interest is the pressure response at higher rates of resistive Ohmic heating. The pressure profiles for Lexan at $\dot{I} = 1$ kA/ns are shown in Figure 19. These profiles show that the Ohmic heating rate has a direct influence on both the channel pressure and the pressure at the shock front, both of which increase with increased current ramp rate. The channel pressure increases strongly with the ramp rate, while the shock pressure increases more weakly. Further, it is also noticeable that at 3 kA/ns, the peak pressure in the channel no longer decreases with time, but increases slightly. All of these effects are also seen in the pressure profiles for water, which are not included here.

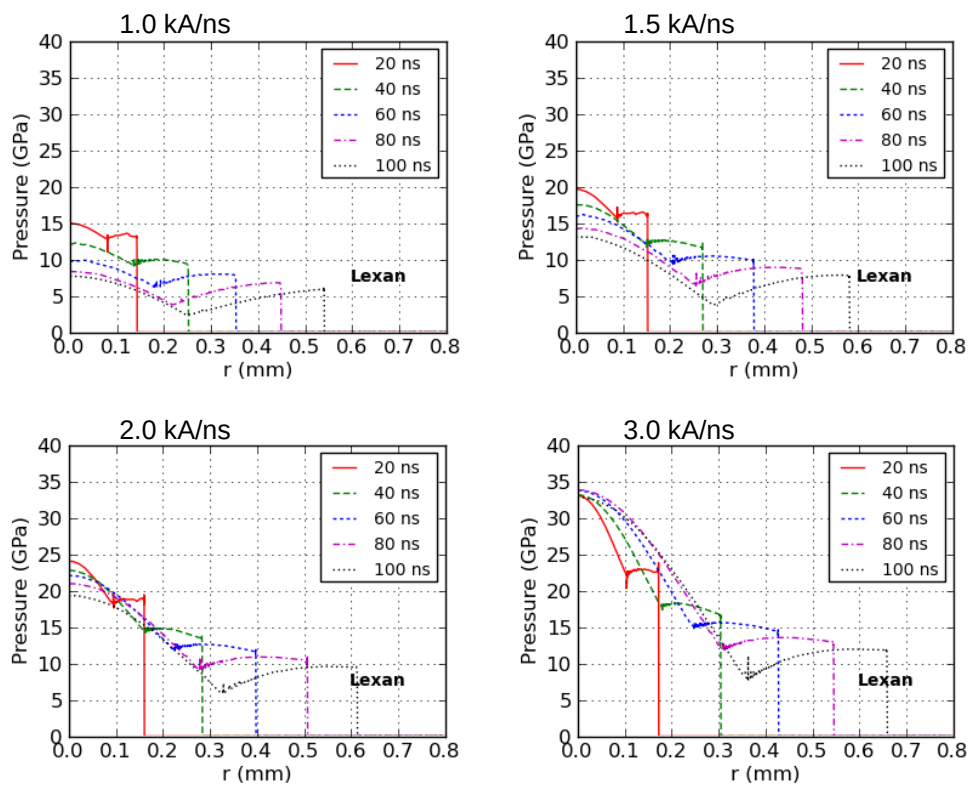

Figure 19: Time snapshots of pressure profiles in Lexan for high current ramp rates.

The mean channel pressure as a function of time is computed for these cases just like the baseline cases, as the arithmetic average of all elements inside the channel-wall location. The mean channel pressure history including the values on axis and at the "boundary" (channel wall) is plotted for these high ramp rates in Figure 20. The channel pressure appears to be both higher and more steadily maintained over time with higher ramp rates.

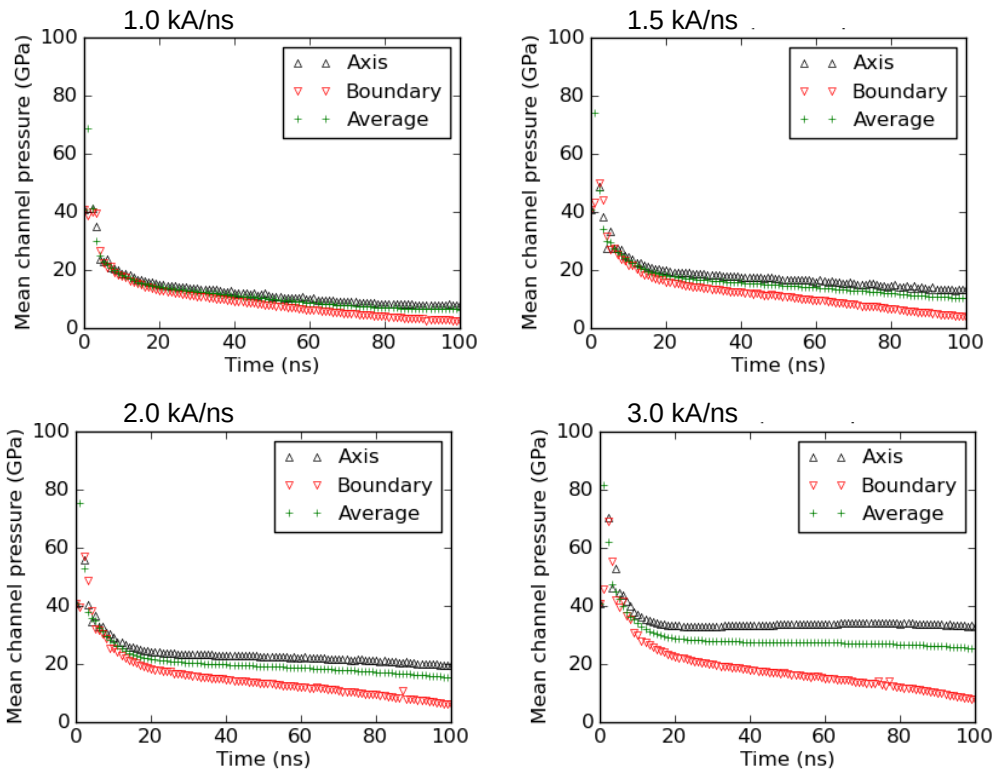

Figure 20: Mean channel pressure $\overline{\boldsymbol{p}}(\boldsymbol{t})$ in Lexan at high current ramp rates.

Table 4: Channel expansion rates (linear fit) and mean coupling coefficient values for Lexan at high current ramp rates.

	Lexan	
	Expansion velocity v_{ch} (m/s)	Coupling coefficient K_p
1.0 kA/ns	2658	1.422
1.5 kA/ns	3032	1.476
2.0 kA/ns	3303	1.554
3.0 kA/ns	3676	1.738

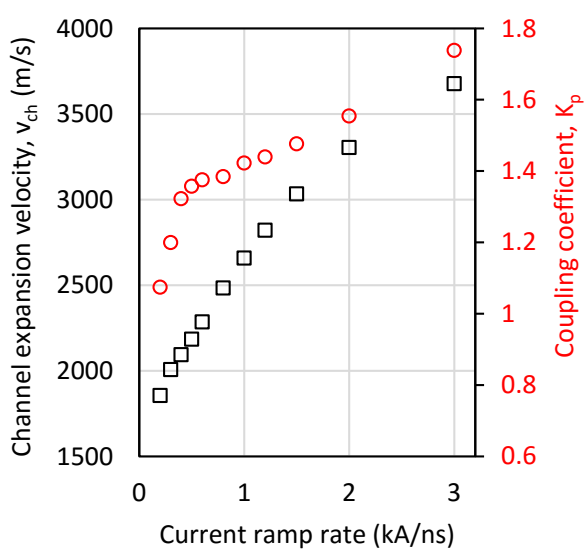

Figure 21: Ramp-rate dependence of Lexan channel expansion velocity $\boldsymbol{v_{ch}}$ and $\boldsymbol{K_p}$.

To characterize the dependence of the mechanical coupling on the current ramp rate for Lexan, the mean values of v_{ch} and K_p are listed in Table 4, and the corresponding data for all current ramp rates $0.2 \leq \dot{I} \leq 3$ are plotted in Figure 21. We see that the current ramp rate has a very strong effect on the channel pressure and rate of expansion. The channel expansion rate grows almost linearly with the ramp rate up to 2 kA/ns. However, the mechanical coupling coefficient also increases with increasing ramp rate. This is due to the very large channel pressures that are seen in Figure 20, but the dependence is not linear. To summarize: channel pressures and expansion rates continue to grow as ramp rates increase beyond 1 kA/ns, but momentum transfer to the medium by the spark channel becomes less efficient.

5.3 Mesh resolution

The calculations shown up to this point were performed using computational meshes with 100 elements spanning the initial channel radius (100-nm resolution). To test whether computed solutions at this mesh resolution are sufficiently mesh-insensitive, one further series of simulations was conducted for water only, using one coarser and two finer meshes – at resolutions of 50, 200, and 400 elements per initial channel radius (element dimensions *dx* = 200, 50, and 25 nm). The same mechanical analysis for channel growth was conducted, so that mesh sensitivity could be studied. In each case, the axial (*z*-) dimension of the mesh was adjusted by the same factor as in the radial (*r*-) dimension, so that the aspect ratio of the elements remained fixed. Volumetric scale factors were adjusted accordingly to account for the change in the resistance and inductance communicated back to the circuit model. Mesh elements outside the initial channel were also refined proportionally.

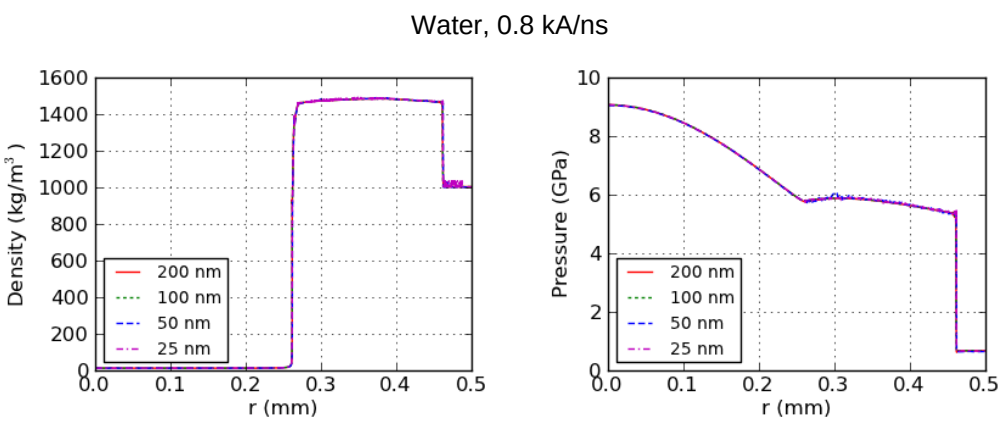

Figure 22: Density (left) and pressure (right) profiles at *t* = 100 ns in water at 0.8 kA/ns, for coarse and fine meshes (*dx* = 200, 100, 50, 25 nm).

The resulting profiles of density and pressure in water for the 0.8-kA/ns case at the final time (*t* = 100 ns) are shown in Figure 22. The baseline case has a resolution of *dx* = 100 nm. The additional coarse- and fine-mesh cases span three doublings of the mesh resolution, but the solution profiles are visibly overlapping. The fine-scale detail of the solution profiles near the shock front is shown in Figure 23. Here we can see that low-level noise in the solution profiles decreases as the mesh is refined, although some oscillations remain at the shock front. Overall, the character of the solutions does not change significantly.

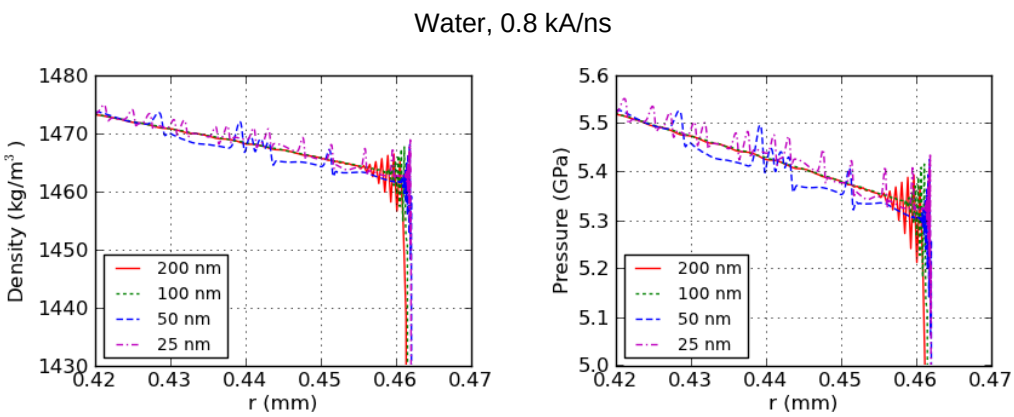

Figure 23: Zoomed-in views of the shock front in density (left) and pressure (right) profiles at t = 100 ns in water at 0.8 kA/ns, for coarse and fine meshes (dx = 200, 100, 50, 25 nm).

The mechanical analysis for computing channel expansion speed, channel pressure, and the mechanical coupling coefficient K_p is repeated again here for each of these meshes and several current ramp rates in water. These data are shown in Figure 24, including the baseline results for dx = 100 nm. The plot shows that the channel expansion velocity v_{ch} appears to approach an asymptotic limit as the mesh is refined, and its variability with the mesh resolution is small, particularly at the larger current ramp rates. For the coupling coefficient K_p, the variability with mesh resolution is larger, particularly at the lower current ramp rates, but in all cases it still does demonstrate monotonic approach toward an asymptotic limit.

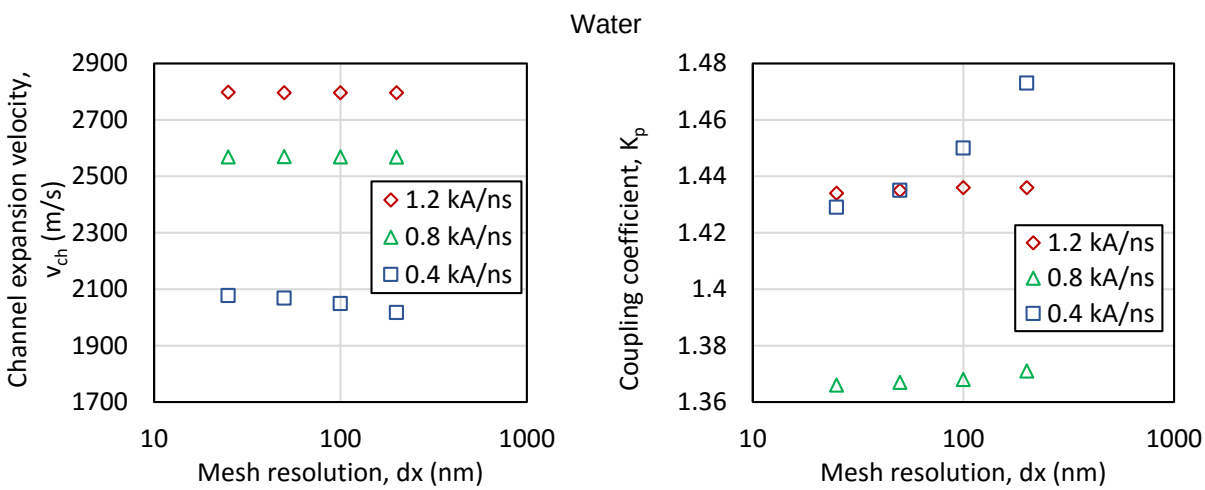

Figure 24: Resolution study for (left) channel expansion velocity and (right) coupling coefficient for water at several ramp rates.

6. CONCLUSIONS

The radiation-MHD simulations conducted in this study examine the growth of spark channels in water and Lexan driven by linearly rising driving current pulses with ramp rates between 0.2 and 3 kA/ns, and the response of the material under these conditions. The simulations predict spark channel expansion velocities up to around 3000 m/s, channel pressures generally in the range of 10-40 GPa, and K_p values mostly between 1.1 and 1.4. These calculations provide a baseline for use in predicting how solid and liquid materials subjected to intense electric discharges are likely to behave and in particularly how they may respond mechanically. The simulations are only one-dimensional, and are based on all of the assumptions inherent in MHD, starting from an assumed pre-formed cylindrical spark channel. But they should allow for the development of a general understanding of what mechanical and thermodynamic environments may be expected in these systems.

In addition to the central series of simulations, several sensitivity studies demonstrate other trends within the models. When a preheated temperature of 250˚C is assumed in the material prior to spark initiation, the modeling shows that the channel development is slightly more energetic, though the changes are not large in magnitude. When current ramp rates exceeding 1 kA/ns, up to 3 kA/ns are applied, the pressure in the channel continues to grow, leading to channel pressures of many tens of GPa, and channel expansion velocities exceeding 3500 m/s. Finally, when the finite-element discretization is refined or coarsened, the results change very little or converge toward an asymptotic limit.

7. REFERENCES

1. A.C. Robinson et al., "ALEGRA: an arbitrary Lagrangian-Eulerian multimaterial, multiphysics code," Proceedings of the 46th AIAA Aerospace Sciences Meeting, Reno, Nevada, January 2008. http://arc.aiaa.org/doi/abs/10.2514/6.2008-1235

2. L.K. Warne, R.E. Jorgenson, J.M. Lehr, "Resistance of a Water Spark," Sandia National Laboratories technical report SAND2005-6994.

3. J.H.J. Niederhaus, K. Cochrane, R.E. Jorgenson, and L.K. Warne, "Computational shock-MHD modeling for lightning blast-through in aeroshells," Sandia National Laboratories technical report SAND2012-2276 (OUO).

4. E. M. Bazelyan and Yu. P. Raizer, *Spark Discharge*. CRC Press, 1998.

5. F. H. Ree, "Equation of State of Water," Lawrence Livermore National Laboratory technical report UCRL-52190, December 1976.

6. S. L. Thompson, "ANEOS Analytic Equation of State for Shock Physics Codes Input Manual," Sandia National Laboratories technical report SAND89-2951, March, 1990.

7. M. P. Desjarlais, "Practical improvements to the Lee-More conductivity near the metal-insulator transition", *Contrib. Plasma Phys.* **41**, 267–270, 2001.

8. B. M. Dobratz, "The insensitive high explosive triaminotrinitrobenzene (TATB): development and characterization," Los Alamos National Laboratory technical report LA-13014-H, August, 1995.

9. L. L. Stevens, N. Velisavljevic, D. E. Hooks, D. M. Dattelbaum, "Hydrostatic compression curve for triamino-trinitrobenzene determined to 13.0 GPa with powder x-ray diffraction," Propellants, Explos., Pyrotech. **33**(4) 286–295, 2008. http://onlinelibrary.wiley.com/doi/10.1002/prep.200700270/full

10. M. M. Gorshkov, K. F. Grebenkin, and A. L. Zherebtsov, "On the physical mechanism of electroconductivity of detonation products of condensed high explosive," AIP Conf. Proc. **849**(201), 2006. http://dx.doi.org/10.1063/1.2337201

11. T. E. Larson, P. Dimas, and C. E. Hannaford, "Electrostatic sensitivity testing of explosives at Los Alamos," Ninth Symposium (International) on Detonation, August 1989. http://www.osti.gov/scitech/servlets/purl/5966858

12. G. I. Kerley and T. L. Christian-Frear, "Prediction of explosive cylinder tests using equations of state from the PANDA code," Sandia National Laboratories technical report SAND93-2131, September 1993. http://www.osti.gov/scitech/biblio/10115447-prediction-explosive-cylinder-tests-using-equations-state-from-panda-code

13. G. I. Kerley, "CTH Equation of State Package: Porosity and Reactive Burn Models," Sandia National Laboratories technical report SAND92-0553, 1992.

APPENDIX A: TATB SPARK CHANNEL SIMULATIONS

A series of simulations is conducted to characterize the development and growth of a spark channel in TATB for current ramp rates between 0.2 and 3 kA/ns. TATB is an insensitive high explosive based on triamino-trinitrobenzene. It is of interest in engineering applications because of its high density, decreased sensitivity to detonation, and high-temperature stability [8,9]. The electrical properties of TATB have not been studied extensively, but Gorshkov *et al*. (2006) have shown that the detonation product gases can carry an electric current [10]. They have also measured a peak electrical conductivity of approximately 350 S/m in the detonation region. Dobratz (1995) [8] quotes an electrical breakdown voltage of 5,750 V/mm for TATB, and notes that TATB did not respond in spark sensitivity tests found in several references, though other explosives did respond. In the only test cited by Dobratz for which information could be found, it appears the current ramp rate is significantly smaller than those studied here [11].

A.1. Approximations for TATB material configuration

For water and Lexan, EOS and electrical/thermal conductivity models are readily available in the material data provided with the ALEGRA code, and from previous work. For TATB, however, there are two barriers to creating a reliable material configuration.

- The first barrier is that although there have been some measurements, there is no well-established electrical conductivity model for any explosive material that spans both the ambient, unreacted state and the state of the detonation products.

- The second barrier is that although EOS models do exist for unreacted solid material and detonation products, the unreacted EOS models generally are only appropriate for solid-state conditions – typically Mie-Grüneisen models. EOS models do not exist for unreacted explosives in the melted or vaporized state.

Since we are interested in the spark channel behavior in TATB before and after detonation, we need a model for the electrical conductivity not just in the ambient, unreacted state but also in the reacted state, *i.e.* for the detonation products. Further, since the spark channel may exist and expand into unreacted material prior to detonation (if it detonates at all), we also need an EOS model for unreacted TATB which allows for heating of the material beyond the solid state.

Therefore, two contrived material setups are used here

(1) "Dense Lexan" refers to an inert TATB surrogate with
   a. The EOS model of Lexan (ANEOS 7751), modified by a constant density scaling factor s_r = 0.6115 applied uniformly during the ALEGRA simulation so that the ambient density of the material is the ambient density of TATB. (The s_r factor is the inverse of the density ratio – see the note below in explanation for Table 5 on details of the s_r factor.)
   b. The LMD Lexan electrical conductivity model, modified by a constant scaling factor s_c = 0.1, reducing the electrical conductivity uniformly during the ALEGRA simulation.

(2) "TATB" refers to an energetic material with

a. The EOS model of Lexan (ANEOS 7751) for the unreacted material, modified by a constant density scaling factor s_r applied uniformly during the ALEGRA simulation so that the ambient density of the material is the ambient density of unreacted TATB.
b. The Sesame 8050 table of Kerley for TATB detonation products, which is ALEGRA's recommended EOS model [12].
c. The LMD Lexan electrical conductivity model, modified by a constant scaling factor $s_c = 0.1$, reducing the electrical conductivity uniformly during the ALEGRA simulation.

Table 5: Material properties and computational material models used in ALEGRA simulations for TATB. Information for water and Lexan from Table 1 is duplicated here for reference.

	Water	**Lexan**	**"Dense Lexan"**	**TATB**
Ambient density (kg/m^3)	1000	1185	1938	1938
Ambient electrical conductivity (S/m)	4.80×10^{-8}	4.33×10^{-8}	2.85×10^{-1}	2.85×10^{-1}
Electrical conductivity (S/m), $T = 1$ eV	1.44×10^{5}	2.14×10^{4}	4.43×10^{3}	4.43×10^{3}
Electrical / thermal conductivity model	LMD customized	LMD "Lexan"	LMD "Lexan", $s_c = 0.1$	LMD "Lexan", $s_c = 0.1$
EOS model	Sesame 7150	ANEOS Sesame 7751	ANEOS Sesame 7751, $s_r = 0.6115$	ANEOS Sesame 7751, $s_r = 0.6115$
EOS model, reaction products	-	-	-	Sesame 8050
Opacity model	Tabular "water"	Tabular "CH"	Tabular "CH"	Tabular "CH"

The details of these configurations for TATB-like materials are shown in Table 5, along with the same information for water and Lexan for reference. The approximations present in these configurations are significant. The density scaling factor $s_r = 0.6115$ is the inverse ratio of the ambient densities of TATB (1938 kg/m^3) and Lexan (1185 kg/m^3), where the ambient TATB density is obtained from the standard ALEGRA Mie-Grüneisen model for "coarse, high density" TATB ("TATB_HD"). This factor (called "SR" in ALEGRA input) is not applied to the density itself, but to the density at which the EOS model is evaluated. It scales the density input to the EOS model so that an EOS can be used for a material of a different density.

The electrical conductivity scaling factor s_c = 0.1 is obtained by trial-and-error testing with ALEGRA spark channel simulations, reducing s_c until a realistic spark channel profile is obtained for the "dense Lexan" scenario. The factor s_c is applied to all of the material in the simulation, interior and exterior to the initial channel, but the thermal conductivity is not modified. Without s_c, no distinct channel wall forms in the simulations. Instead, the conductivity remains anomalously high on the channel periphery during expansion, resulting in lower Joule heating, lower temperature, higher density, and ultimately a density profile across the channel that does not coincide with channel behavior seen in previous work for other materials [2]. This high conductivity most likely results from the fact that Lexan has a much lower ambient density than TATB. By evaluating the Lexan LMD conductivity model at the density of TATB with a given temperature, one obtains a conductivity for a density that is unrealistically high. The scaling factor s_c is an attempt to compensate for this effect. It directly modifies the conductivity value itself, not the density at which the conductivity model is evaluated – in this way it is much different from the density scaling factor s_r.

Lowering the conductivity of the material increases the rate of Joule energy deposition by the spark channel. Further, it lowers the ramp rate required for detonation of TATB. Without this change, the results are anomalous so that no mechanical analysis can be done for "dense Lexan," and no spark channel appears for TATB. Since the present study is intended to look at the effects of spark channel formation, assuming they form, the simulations were conducted under these approximations as an initial attempt to characterize these systems.

The use of the Lexan LMD model for TATB is loosely justified by the similar hydrocarbon-based composition of the two materials. This also provides a loose justification for use of the Lexan EOS in the "dense Lexan" scenarios as an inert surrogate for TATB. As with Lexan, the "CH" Tabular Opacity model is used here for both "dense Lexan" and TATB.

A final approximation is that for TATB (not dense Lexan), the Joule heating term in ALEGRA is disabled for densities smaller than 300 kg/m^3, using the "Joule heat density floor" option. Without this change, for cases with detonation, extraordinarily intense Joule heating drives an abrupt decrease in density which reduces the stable timestep to prohibitively small values.

All of these approximations together leave us with a series of simulations for spark channels in TATB which may provide qualitative insight but not firm predictive assessment.

A.2. Dense Lexan and TATB solution profiles

The ALEGRA simulations are conducted for dense Lexan and TATB using the same conditions and material configurations described above for water and Lexan, at current ramp rates of 0.2, 0.3, 0.4, 0.5, 0.6, 0.8, 1.0, and 1.2 kA/ns. Representative solution profiles in density are plotted in Figure 25, showing the system evolution through t = 100 ns.

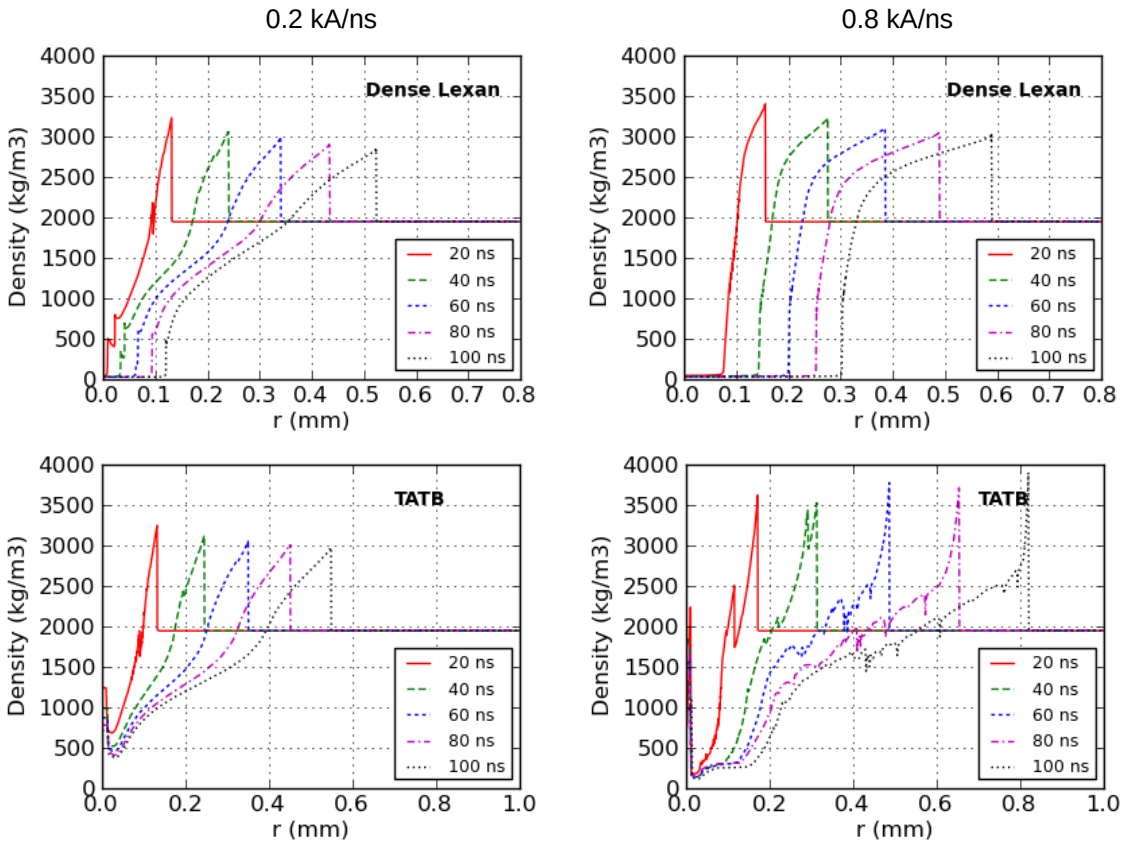

Figure 25: Time snapshots of dense Lexan and TATB density profiles computed by ALEGRA for the 0.2 and 0.8 kA/ns cases.

Similar to the results for water and Lexan in Section 4.1, a characteristic spark channel evolution can be seen in the dense Lexan and TATB solution profiles. The high-temperature channel at initialization expands quickly and drops to low density. However, it does not collapse to densities as low as those seen in water and Lexan, particularly at the lowest current ramp rate of 0.2 kA/ns. A distinct channel wall forms and a shock wave propagates outward into undisturbed material. The peak density and the rate of expansion both increase as the current ramp rate increases.

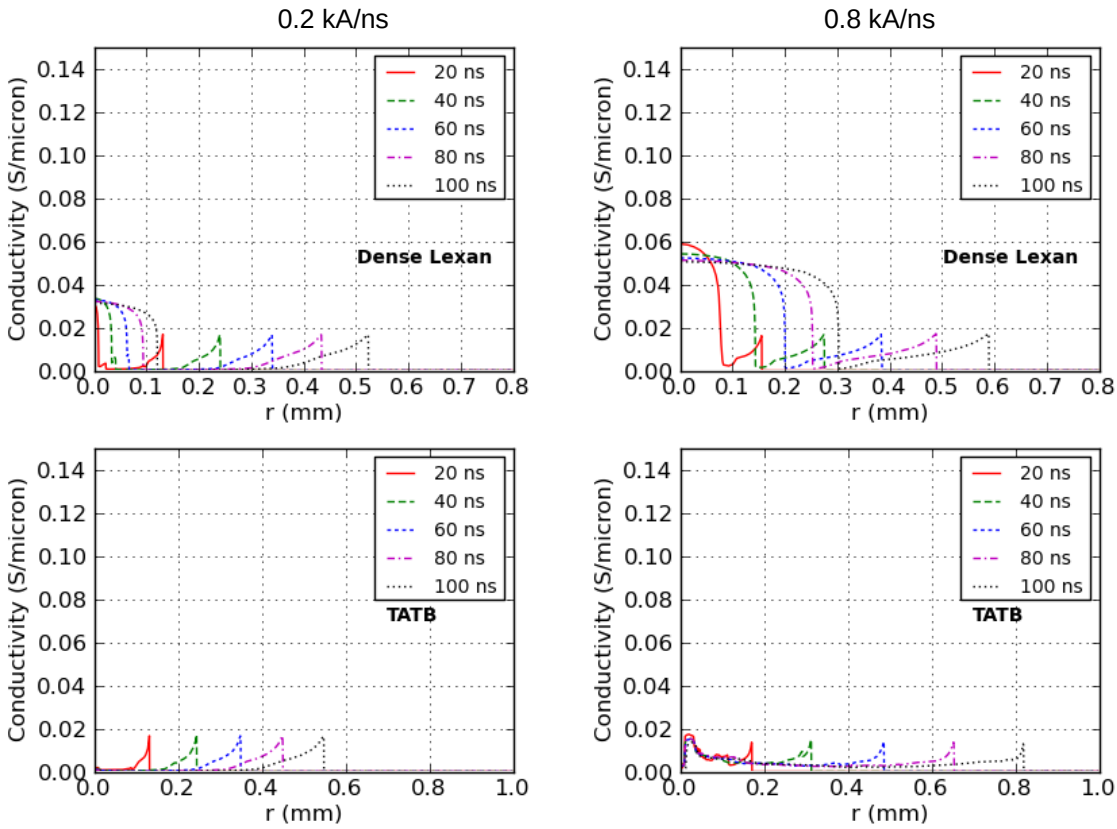

Figure 26: Time snapshots of dense Lexan and TATB electrical conductivity profiles computed by ALEGRA for the 0.2 and 0.8 kA/ns cases.

The corresponding profiles in electrical conductivity are shown in Figure 26. For dense Lexan, the electrical conductivity profiles show a characteristic expanding region of conductive material in the channel, though at a much lower conductivity than in water or Lexan (partially due to the s_c factor). For dense Lexan, the boundary of the conducting region coincides with the density jump, as seen previously. In these materials, however, the conductivity jump associated with the shock is quite significant, so that some current can be expected to flow well outside the low-density, high-temperature channel. Further, for TATB, the central conducting region is absent at low ramp rates, and the shock conductivity is still very prominent at the high ramp rates. This makes it impossible to measure a channel radius for TATB without relying completely on the density profile. Since the current is likely to be flowing outside of the low-density region, it does not make sense to do this. Therefore, we obtain no channel expansion rates or K_p values here, other than for the "dense Lexan" surrogate.

We also note that the electrical conductivity magnitude for TATB is very large compared to the value of 350 S/m measured by Gorshkov *et al*. (2006) for the detonation products in shock-driven detonation – shown in Figure 1 of their paper [10]. For TATB here with an electric-spark driver, we are seeing on the order of 10,000 S/m, even with the use of the s_c scale factor.

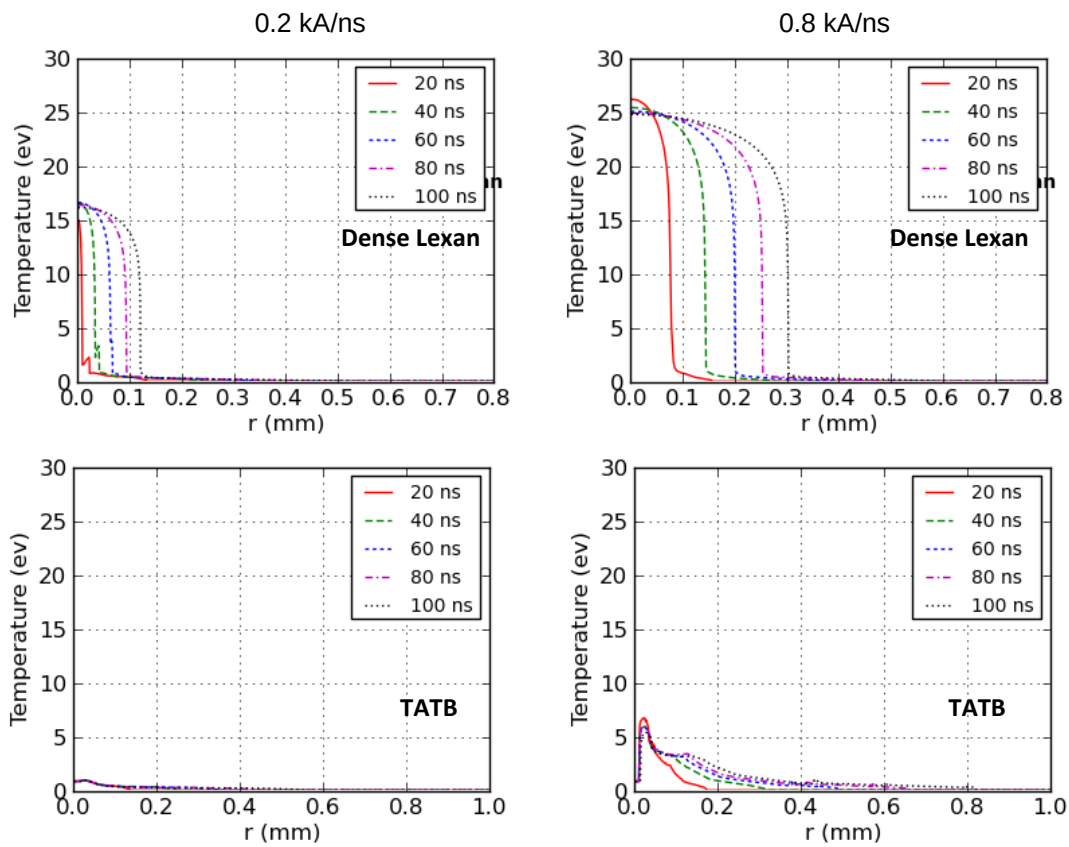

Figure 27: Time snapshots of dense Lexan and TATB temperature profiles computed by ALEGRA for the 0.2 and 0.8 kA/ns cases.

Temperature profiles for the inert dense Lexan and energetic TATB cases are shown in Figure 27. We see that the temperature in the channel reaches levels on the order of 10 eV or 100,000 K for dense Lexan, but remains much cooler for TATB. It is not clear why temperatures remain relatively so small for TATB. Analysis of the volumetric rate of Joule heating shows that the deposition of energy by the current discharge is no smaller for TATB than for dense Lexan, so it is likely not caused by the Joule heat density floor. (The detonation-zone temperatures measured by Gorshkov *et al*. (2006) – shown in Figure 2 of their paper – are around 2,500 K.)

Associated with these very high temperatures are high pressures, which drive the mechanical impulse to the material generated by the spark event. Pressure profiles for these scenarios are shown in Figure 28. The channel mean pressure and shock wave pressure both appear to be on the order of tens of GPa or hundreds of kilobar. As expected, the channel pressure and shock pressure both grow with increasing current ramp rate.

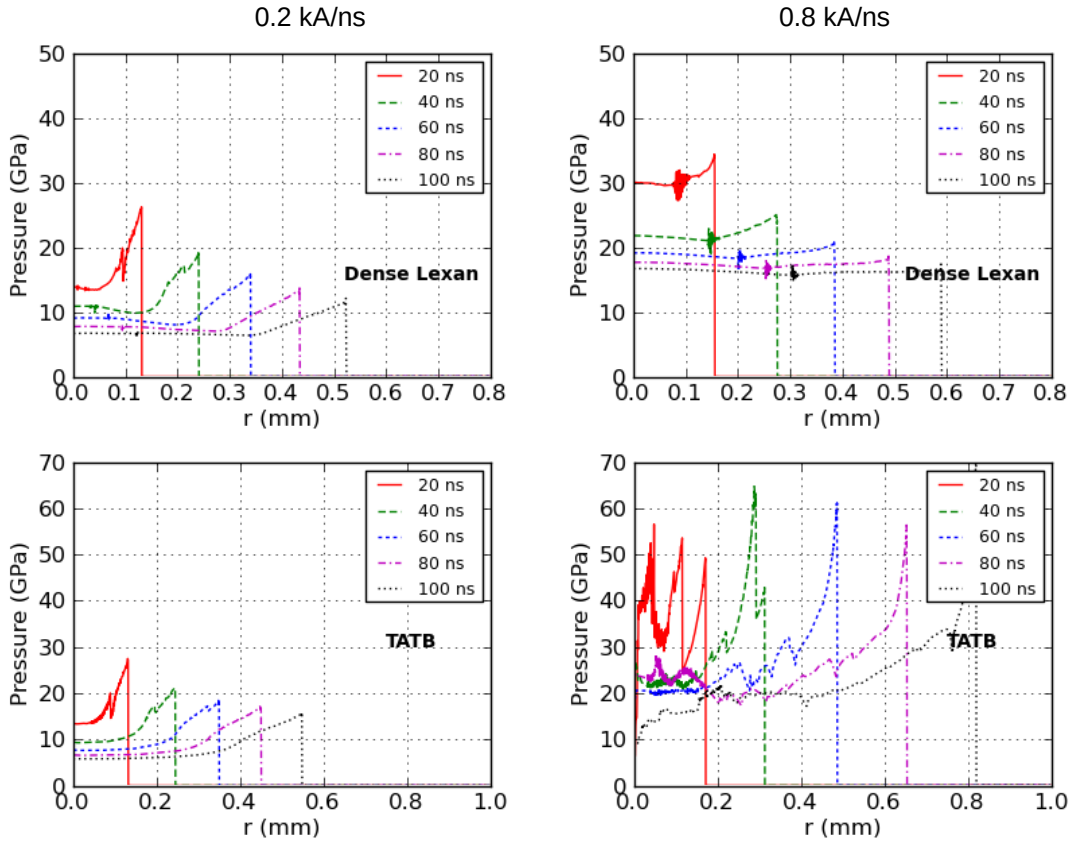

Figure 28: Time snapshots of dense Lexan and TATB pressure profiles computed by ALEGRA for the 0.2 and 0.8 kA/ns cases.

A.3. Extent-of-reaction profiles for active TATB

In the TATB simulations, the history variable reactive burn (HVRB) model is used to capture the detonation physics, so we can examine the evolution of detonation in the material. The "coarse high-density" (TATB_HD) parameterization for HVRB is used here (modified to use the ANEOS 7751 EOS model for unreacted material, as described above). In HVRB, the material is transitioned from the unreacted to the reacted EOS during detonation. The rate of reaction is controlled by the reaction threshold pressure P_I, the calibration pressure scale P_R, and the time scale τ_0 [13]. For TATB_HD, they are defined as P_I = 1 GPa, P_R = 13.5 GPa, and τ_0 = 1 μs. Stevens *et al.* (2008) [9] quote a Chapman-Jouguet pressure of approximately 26 GPa. Therefore, there is a finite chance that detonation will occur, since pressures shown in Figure 28 do reach into the range of these values, though they are sustained for only fractions of a microsecond.

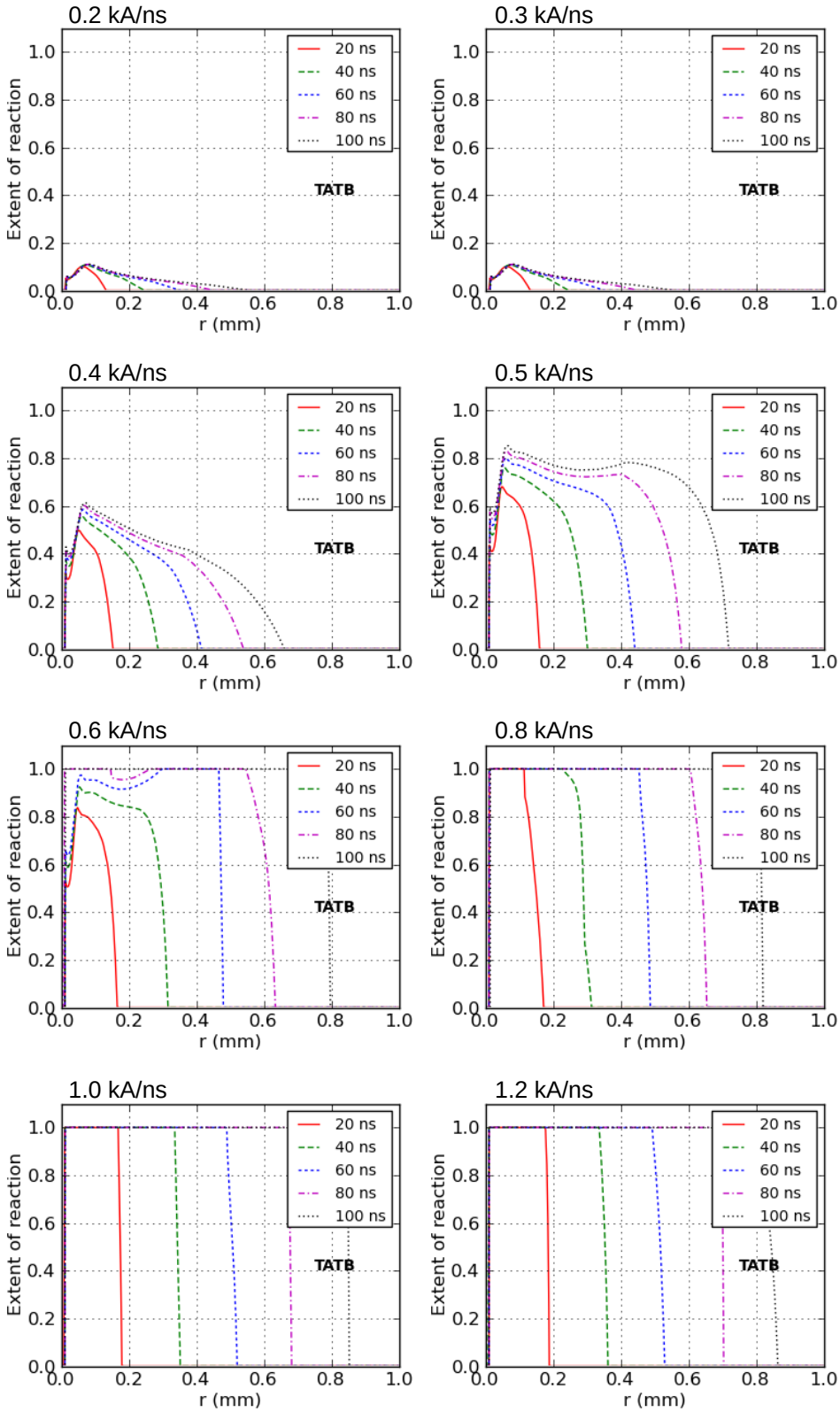

Figure 29: Profiles of the extent of reaction for TATB for a range of current ramp rates.

The HVRB model provides a dimensionless history variable $0 \leq \phi \leq 1$ that tracks the extent of reaction. Profiles of the extent of reaction ϕ for the TATB simulations at several current ramp rates are shown in Figure 29. We see that the current ramp rate has a strong influence on whether and how quickly the material reaches detonation. Full detonation prior to 100 ns occurs for current ramp rates of 0.6 kA/ns and above. At the very high ramp rates, detonation is driven completely by the shock, and the detonation front moves with the shock wave. As mentioned above, these simulations can only be regarded as a qualitative depiction of the development of this system, due the approximations that have been incorporated.

A.4. Channel mechanical analysis for dense Lexan

The mechanical interaction between the spark channel and the medium is analyzed for the dense Lexan cases, like for the water and Lexan simulations. The conductivity jump is used again to locate the channel radius. The resulting channel expansion history and mechanical coupling coefficient K_p values are shown for current ramp rates 0.4 and 0.8 kA/ns in Figure 30 and Figure 31. (The expansion speeds and pressures are not shown.) We see for dense Lexan that the expansion speeds and K_p values, and their trends differ modestly from those found for water and Lexan. The full set of linear-fit expansion velocities and mean K_p values at $25 \leq t \leq 45$ ns for dense Lexan are shown in Table 6. The current ramp rate of 0.4 kA/ns is used instead of 0.2 kA/ns in the plots, because the density profile at 0.2 kA/ns leads to anomalously small channel expansion speeds and large values of K_p, as seen in Table 6.

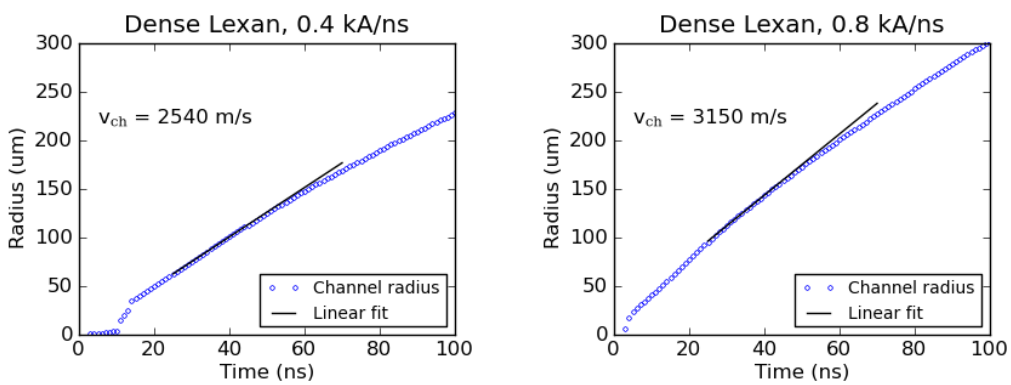

Figure 30: Channel radius $a(t)$ for dense Lexan at 0.4 and 0.8 kA/ns.

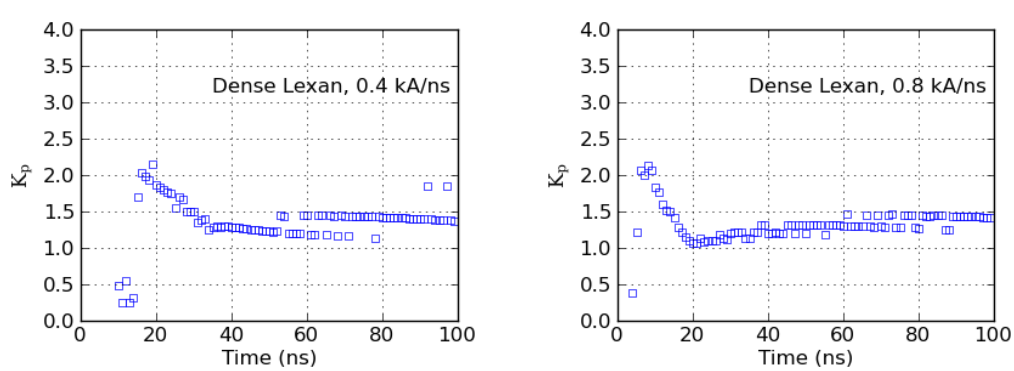

Figure 31: Channel mechanical coupling coefficient K_p for dense Lexan at 0.4 and 0.8 kA/ns.

Table 6: Channel expansion rates (linear fit) and mean coupling coefficient values for dense Lexan.

	Dense Lexan	
	Expansion velocity v_{ch} (m/s)	Coupling coefficient K_p
0.2 kA/ns	1334	3.497
0.3 kA/ns	2054	1.800
0.4 kA/ns	2054	1.368
0.5 kA/ns	2540	1.194
0.6 kA/ns	2813	1.174
0.8 kA/ns	3150	1.190
1.0 kA/ns	3354	1.200
1.2 kA/ns	3548	1.197

For "dense Lexan," in general (except at 0.2 kA/ns), the expansion speeds are modestly higher, and K_p values modestly lower than for water and Lexan, except for the very lowest current ramp rates – generally around a value of 1.2. The shock wave pressure generated by the spark event is noticeably higher in this inert TATB surrogate material than in water or Lexan. This is visible by comparing the pressure profiles in Figure 28 to those in Figure 5. The more intense shock environment produced in "dense Lexan" is likely responsible for the greater expansion speeds, and lower values of K_p. However, the details of this shock environment are strongly constrained by the EOS model used. Since the "dense Lexan" EOS is actually only a modified Lexan EOS, it is not clear how accurate this prediction is. The Mie-Grüneisen EOS model for unreacted TATB would produce a much more reliable shock state, based on measured Hugoniot data, but this EOS cannot be used here, as mentioned above, due to non-solid unreacted states.

A.5. Channel preheat analysis for dense Lexan and TATB

To correspond with the analysis in Section 5.1, an additional series of simulations is conducted for dense Lexan and TATB with an initial temperature of 250˚C in the material exterior to the initial channel. The initial, preheated density at ambient pressure is 1788 kg/m^3 for dense Lexan and TATB. Otherwise the simulations are unchanged from the original series. The resulting profiles of density and temperature for a selected current ramp rate of 0.8 kA/ns are shown in Figures 32 and 33, along with the ambient-temperature results duplicated for reference.

Similar to the results for Lexan, we see here that preheating in "dense Lexan" seems to produce a more energetic spark channel than is seen for ambient conditions. The peak densities are slightly lower, but the temperatures and apparent shock wave speeds are slightly higher. This is not the case for the TATB simulations, which appear to have a spark channel that is somewhat less energetic when preheating is used. For TATB, the outgoing shock wave is noticeably slower with preheat, and the temperatures in the channel are also generally lower.

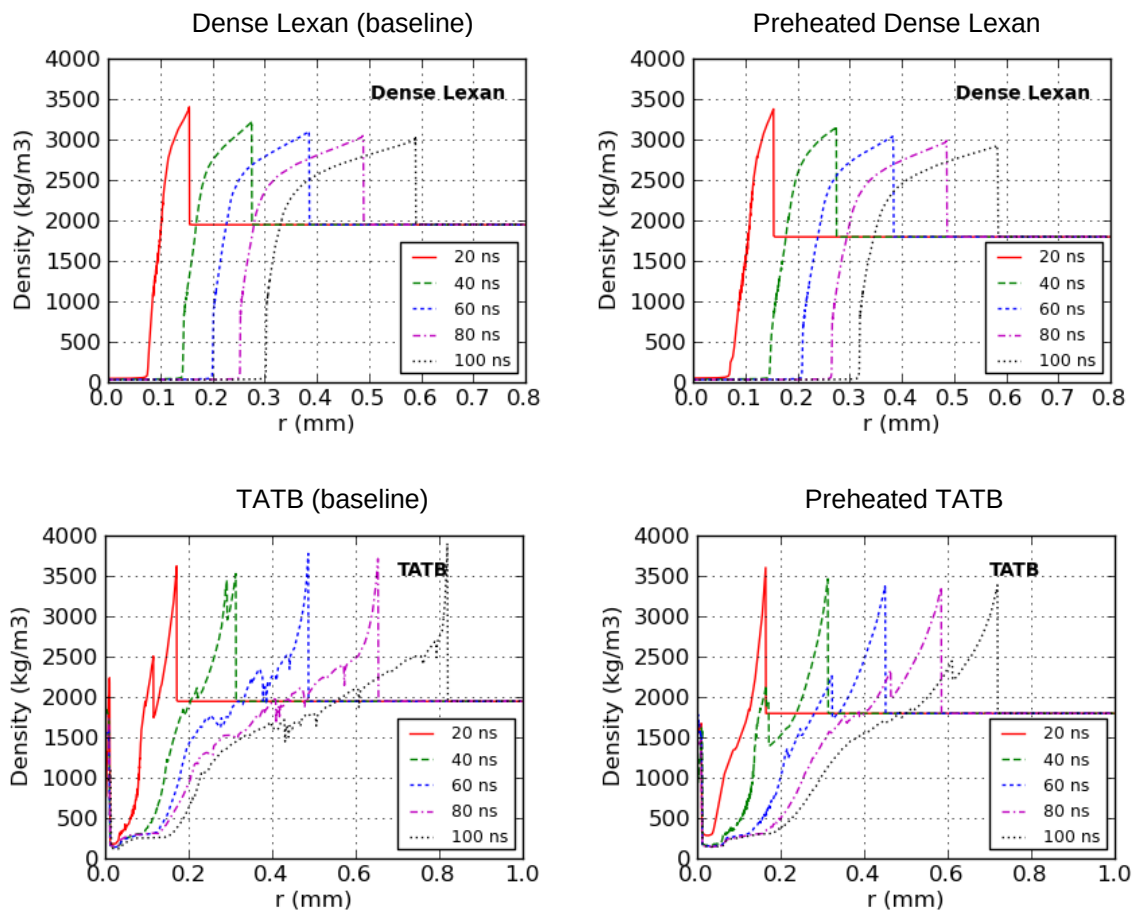

Figure 32: Time snapshots of density computed by ALEGRA for the 0.8 kA/ns case at baseline (left) and with an initial preheated temperature of 250˚C (right).

The mechanical analysis techniques based on detecting the time-dependent channel wall location are applied again here for the dense Lexan scenarios with preheating. Histories of the channel expansion and the mechanical coupling coefficient K_p for dense Lexan with preheating are shown in Figure 34 for 0.8 kA/ns. These can be compared to the data plotted above in Figures 30 and 31. For 0.8 kA/ns, the expansion speed is significantly higher, and the coupling coefficient is significantly lower, indicating a more energetic spark channel when preheating is applied. The complete set of data for all current ramp rates with preheat in dense Lexan is shown below in Table 7. The data for ambient initial conditions are also shown for reference. We see that at all of these ramp rates except 0.2 kA/ns, this observation holds. With preheating, the channel grows faster and the mechanical coupling is stronger (lower K_p) with preheat. This effect is noticeably greater in magnitude for dense Lexan than for Lexan.

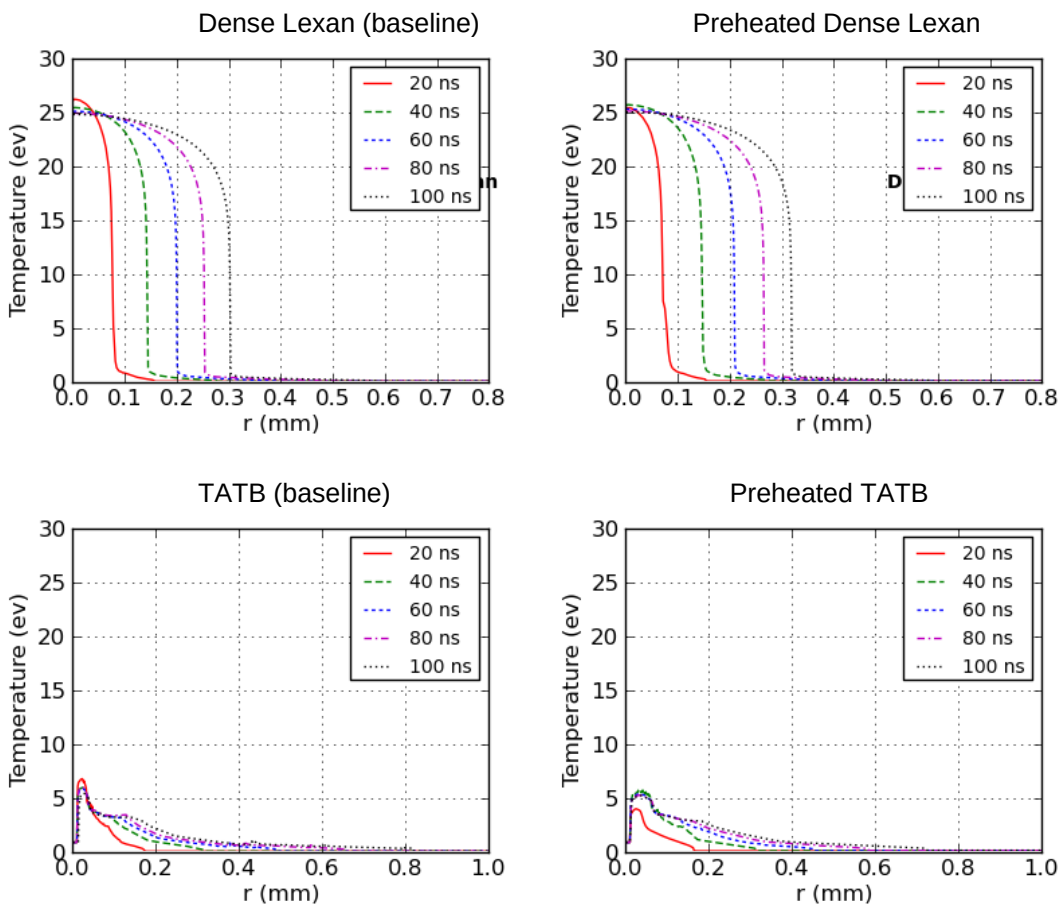

Figure 33: Time snapshots of temperature computed by ALEGRA for the 0.8 kA/ns case at baseline (left) and with an initial preheated temperature of 250˚C (right).

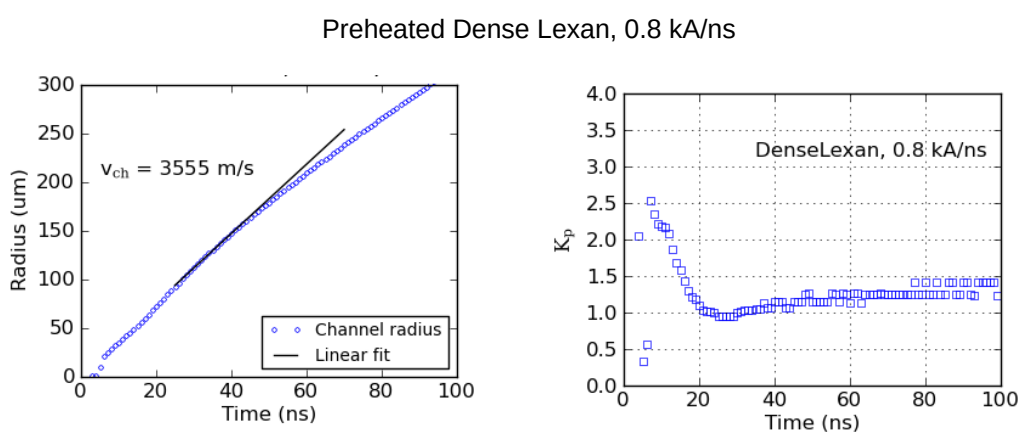

Figure 34: Channel expansion history (left) and mechanical coupling coefficient K_p (right) for dense Lexan for the 0.8 kA/ns case with an initial preheated temperature of 250˚C.

Table 7: Channel expansion rates (linear fit) and mean coupling coefficient values for dense Lexan at baseline and with an initial preheated temperature of 250˚C.

	Dense Lexan (baseline)		**Preheated Dense Lexan**	
	Expansion velocity v_{ch} (m/s)	Coupling coefficient K_p	Expansion velocity v_{ch} (m/s)	Coupling coefficient K_p
0.2 kA/ns	1334	3.497	2038	2.136
0.3 kA/ns	2054	1.800	2696	1.521
0.4 kA/ns	2054	1.368	2693	1.511
0.5 kA/ns	2540	1.194	3139	1.170
0.6 kA/ns	2813	1.174	3403	1.032
0.8 kA/ns	3150	1.190	3555	1.039
1.0 kA/ns	3354	1.200	3638	1.101
1.2 kA/ns	3548	1.197	3782	1.131

For TATB, however, since the shock produced by the spark channel is weaker, the detonation progress is also slower when the material is pre-heated. To see this, the extent of reaction from the HVRB model from the preheated simulations is shown in Figure 35. We see that the extent of reaction is slightly lower overall when the material is preheated, in comparison to the ambient-temperature profiles shown in Figure 29. Nevertheless, the threshold current ramp rate for detonation ($\phi = 1$ anywhere in the domain) remains at 0.6 kA/ns for the preheated case.

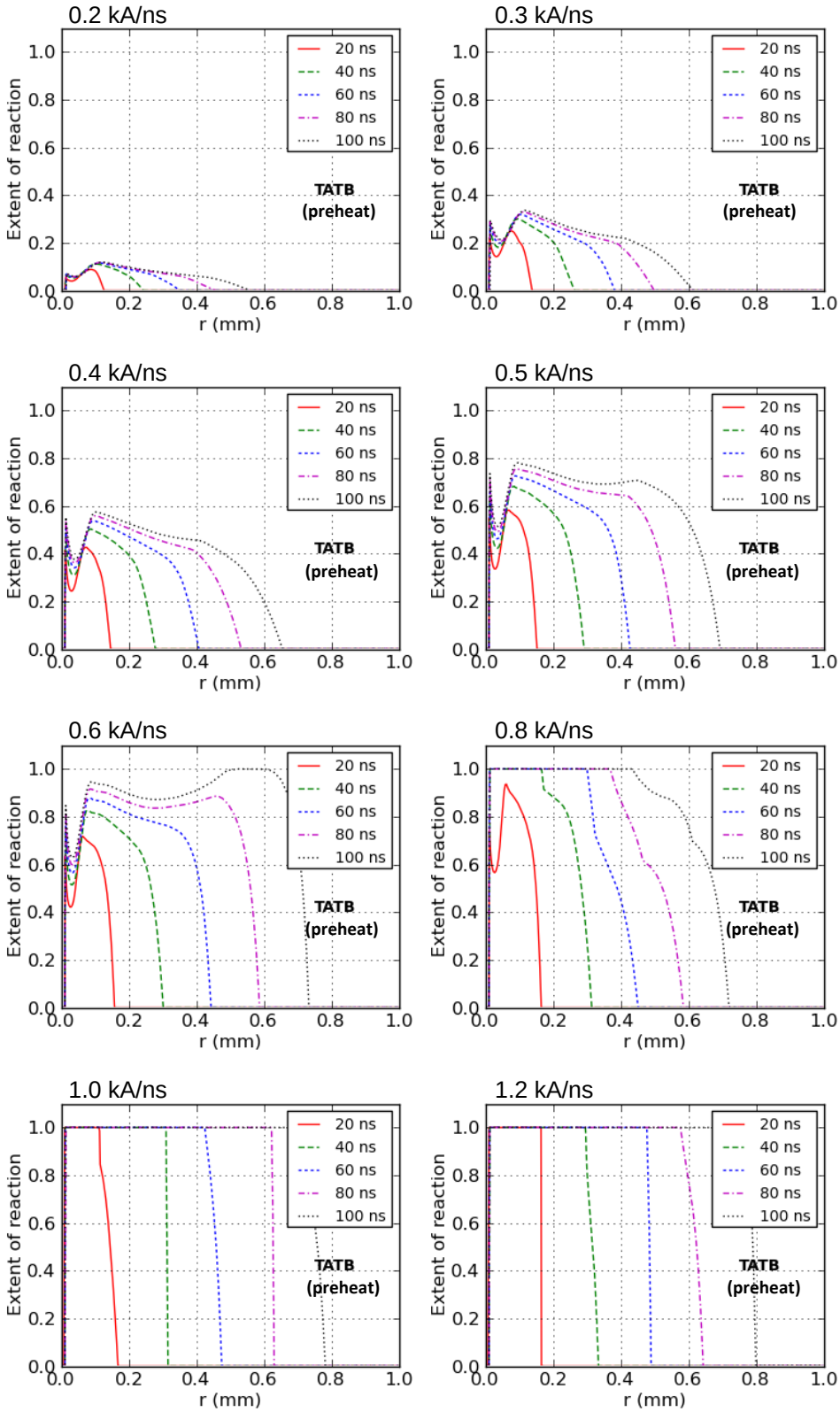

Figure 35: Profiles of the extent of reaction for TATB for a range of current ramp rates an initial preheated temperature of 250˚C.

A.6. Large ramp rates for dense Lexan

To study the effect of higher current ramp rates, the dense Lexan cases are rerun with ramp rates of 1.5, 2, and 3 kA/ns, and all other settings identical to the previous baseline scenarios. Of particular interest is the pressure response at higher rates of resistive Ohmic heating. Profiles of pressure for dense Lexan at high current ramp rates are shown in Figure 36. We see that, like the results for Lexan in Figure 19, the pressure shows a strong dependence on the spark channel current ramp rate. The pressures are much larger in dense Lexan, but the channel pressure still increases strongly with the ramp rate. The shock pressure and speed increases also, but more weakly.

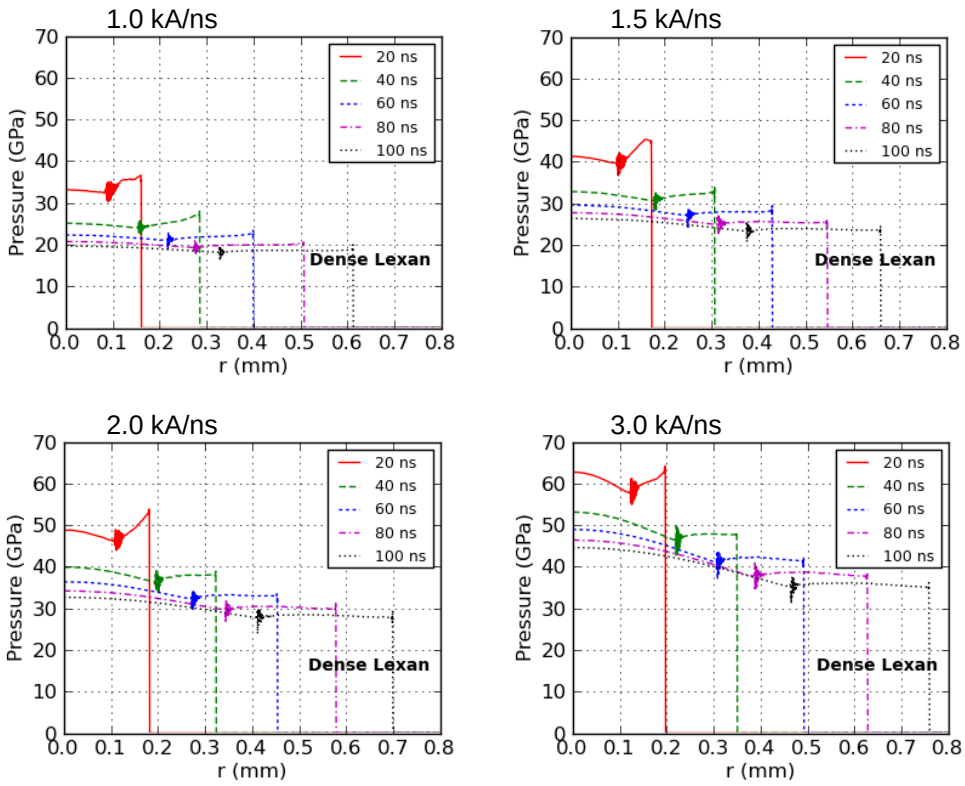

Figure 36: Time snapshots of pressure profiles in dense Lexan for high current ramp rates.

The mean channel pressure as a function of time is computed for these cases as in the baseline cases, using an arithmetic average of all elements inside the channel wall. The mean channel pressure history for dense Lexan at high ramp rates, including the values on axis and at the channel wall ("boundary") is plotted for these high ramp rates in Figure 37. The channel pressure appears to be both higher and more steadily maintained over time with higher ramp rates, and it is very significantly larger than the values for Lexan.

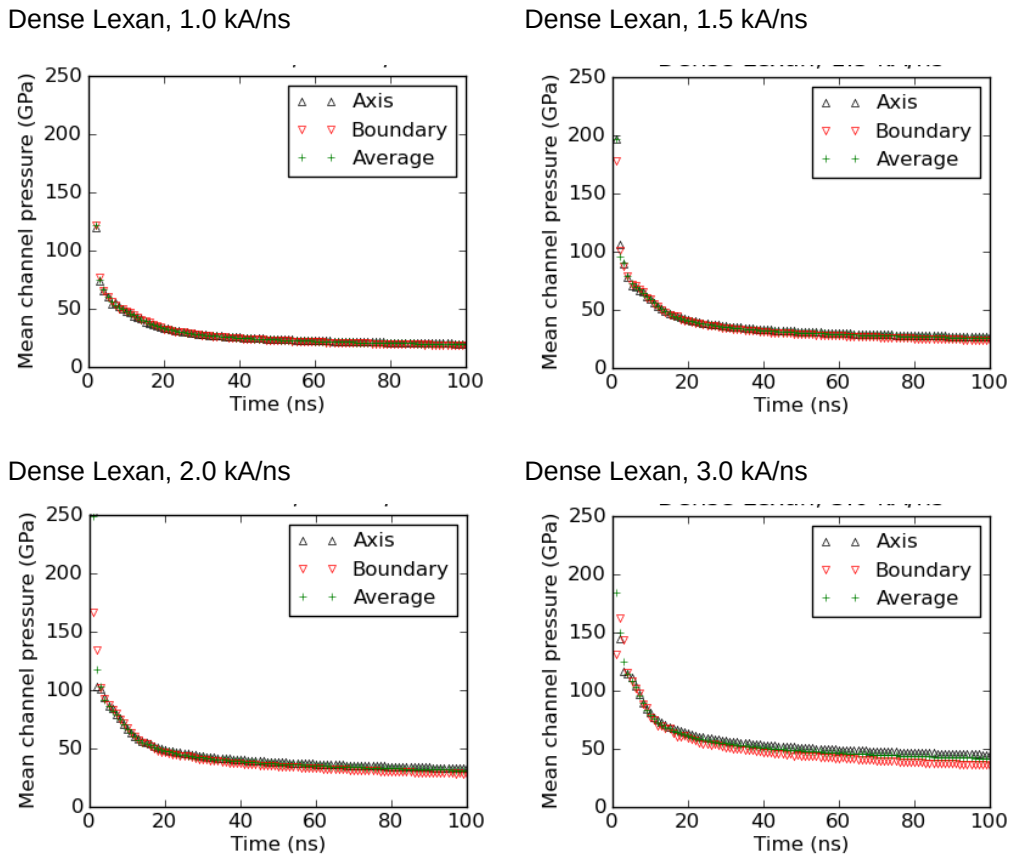

Figure 37: Mean channel pressure $\overline{\boldsymbol{p}}(\boldsymbol{t})$ in dense Lexan at high current ramp rates.

A.7. Mesh resolution study

Finally, we note that simulations using HVRB and other reactive burn models are often subject to strong mesh sensitivity. Very fine meshes are often required to obtain mesh-independent results, particularly in threshold situations where detonation may or may not occur. As was done for the water and Lexan simulations, the TATB simulations here are also examined with a mesh sensitivity study. For all current ramp rates $0.2 \leq \dot{I} \leq 1.2$ kA/ns, the baseline TATB simulations at dx = 100 nm (100 elements spanning the channel) are repeated for mesh resolutions dx = 200, 50, and 25 nm. In particular, the response of the detonation is of interest here. The resulting profiles of the density and pressure for a selected current ramp rate of 0.4 kA/ns are shown here in Figure 38. We see that there is very little variability in the dynamics of the simulation over this very wide range of mesh intervals. Further, the detonation behavior is examined by plotting profiles of the TATB extent of reaction at t = 100 ns for 0.4 and 0.6 kA/ns in Figure 39. We see that variability only appears near the detonation front, within the reaction zone for the 0.6 kA/ns case. Otherwise the detonation results are nearly invariant under mesh refinement, and we can most likely assume that the ramp-rate threshold for onset of detonation is also invariant.

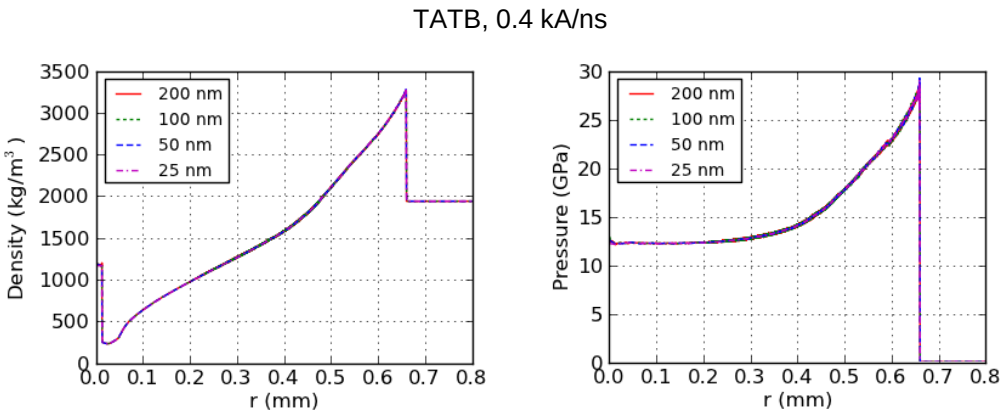

Figure 38: Density (left) and pressure (right) profiles at t = 100 ns in water at 0.8 kA/ns, for coarse and fine meshes (dx = 200, 100, 50, 25 nm).

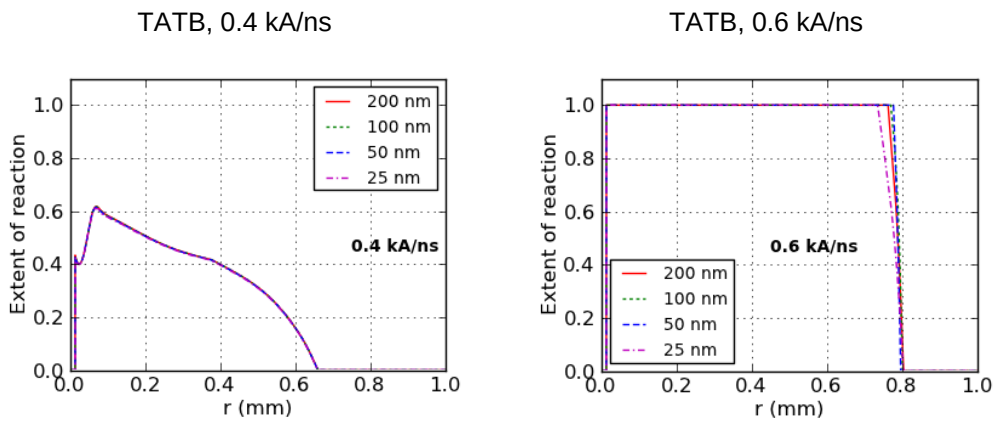

Figure 39: Profiles of TATB extent of reaction at t = 100 ns at (left) 0.4 kA/ns and (right) 0.6 kA/ns, for coarse and fine meshes (dx = 200, 100, 50, 25 nm).

A.8. Dense Lexan and TATB summary

To summarize the examination of modeling for spark channels in TATB and the inert "dense Lexan" surrogate, major approximations are needed in order to produce meaningful results for TATB. These approximations are necessary because of the lack of data for this material under these conditions. Specifically, an equation of state model for unreacted TATB in the liquid and vapor state would be needed, and an electrical/thermal conductivity model for TATB reactants and detonation products in all phases would be needed. Both of these pieces of information would be extremely difficult and costly to provide; therefore, we are left with the approximate scoping calculations generated here.

These scoping calculations suggest that pressures in the range of tens of GPa and channel expansion rates exceeding 3 km/s can be expected for spark events of this type in TATB, resulting in coupling coefficient (K_p) values around 1.2. In the scoping simulations, detonation only occurs in TATB under the stated material-modeling assumptions for current ramp rates of 0.6 kA/ns and above. Preheating the material leads to a more energetic channel for the inert "dense Lexan" surrogate, but a less energetic channel for TATB. However, the 0.6-kA/ns threshold is unchanged with preheat. At much higher ramp rates, up to 3 kA/ns, the channel pressure continues to increase, reaching into the range of hundreds of GPa or megabar. Finally, the study shows that the mesh resolution does not have a significant effect on the results. A final recommendation from this study is that much more useful results could be produced if conductivity models for TATB could be generated, including both the unreacted form and the reaction products.

APPENDIX B: REFERENCE SIMULATION DATA

Several sets of additional solution profile plots and histories from the ALEGRA simulations for water and Lexan at 1, 2, and 3 kA/ns are provided here for reference. In all cases, the exterior material is initialized at ambient conditions (no preheat) – these correspond to the simulations discussed in Sections 4 and 5.2.

B.1. Density profiles

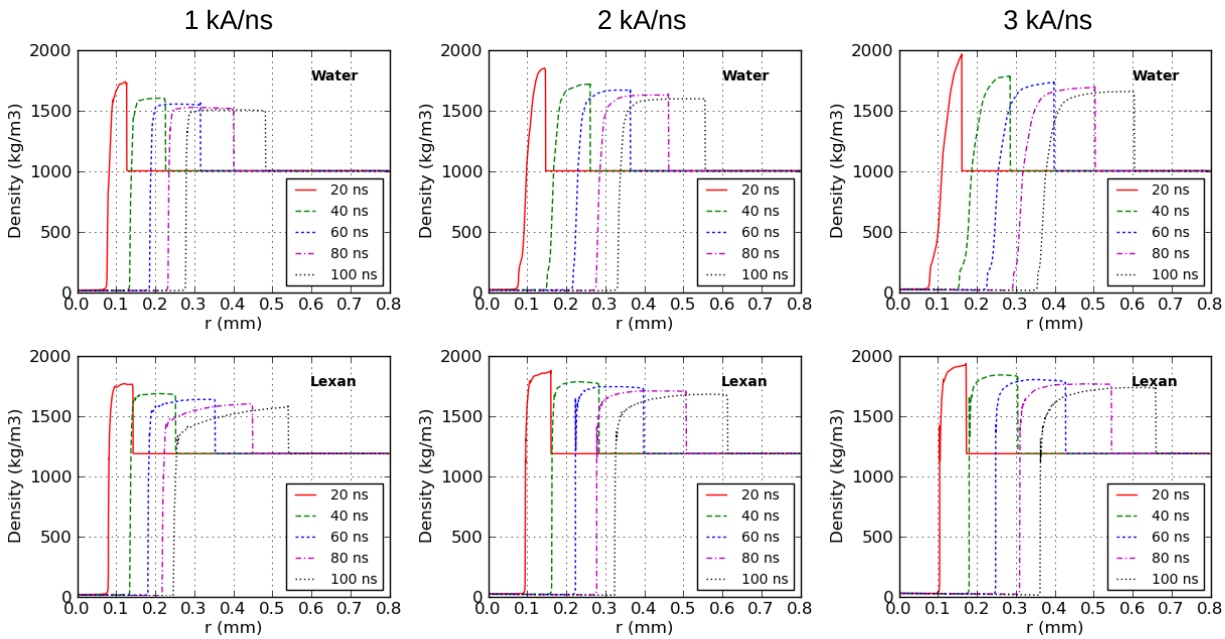

Figure 40: Density profiles for water (above) and Lexan (below).

B.2. Temperature profiles

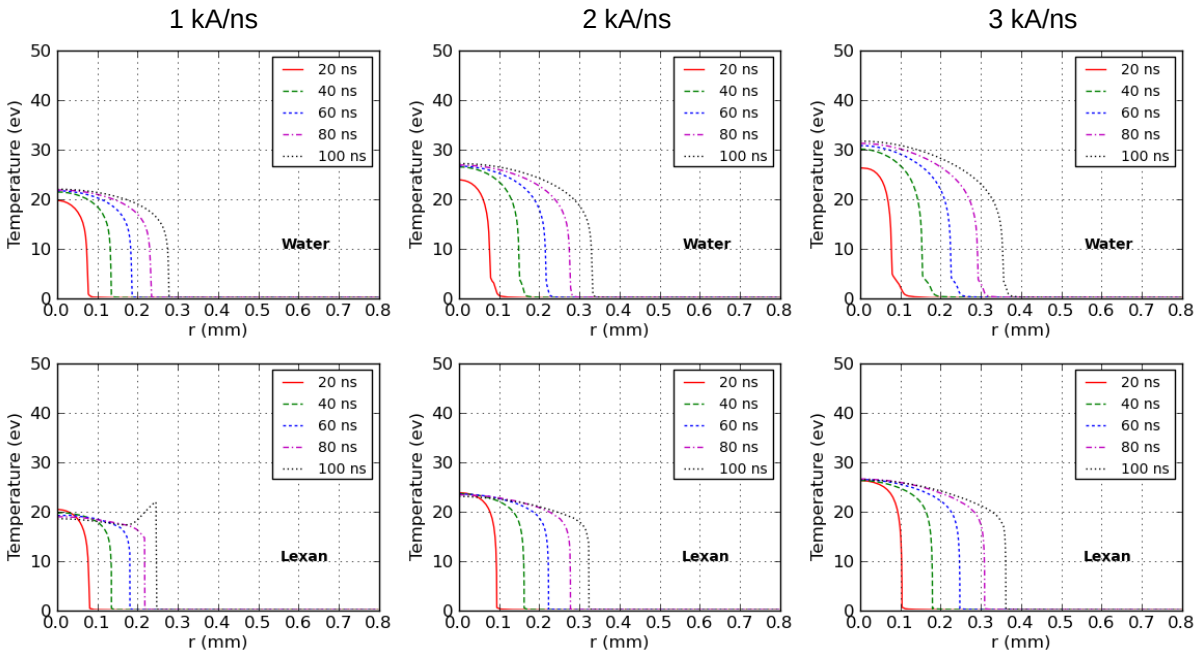

Figure 41: Temperature profiles for water (above) and Lexan (below).

B.3. Pressure profiles

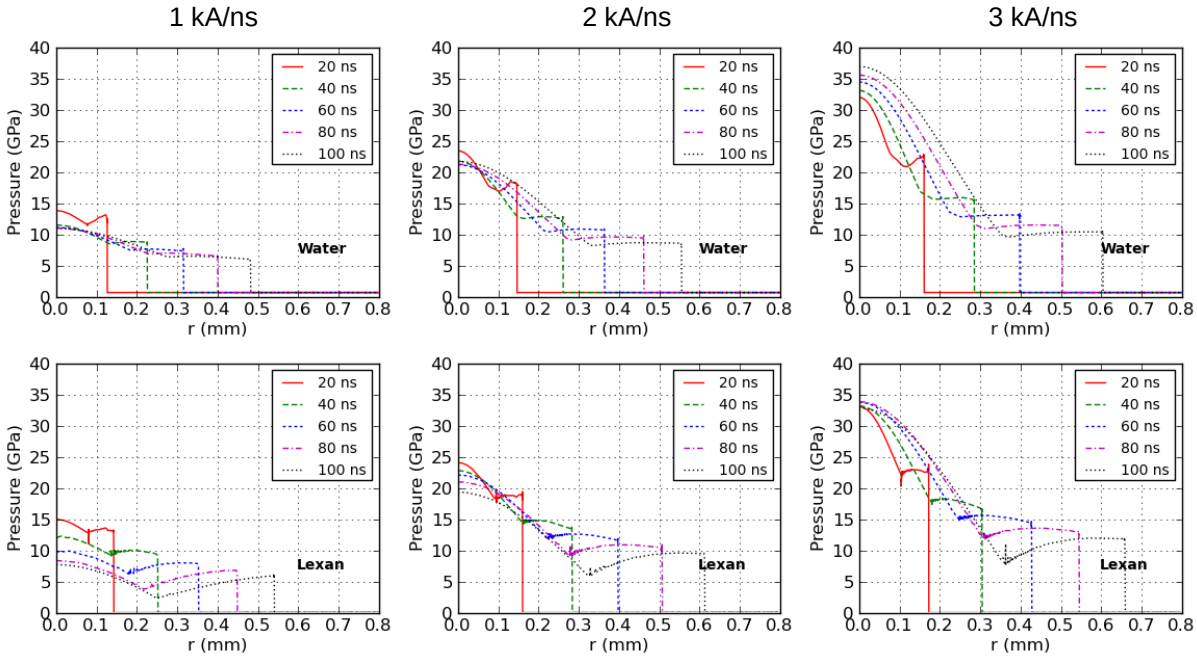

Figure 42: Pressure profiles for water (above) and Lexan (below).

B.4. Mean channel pressure histories

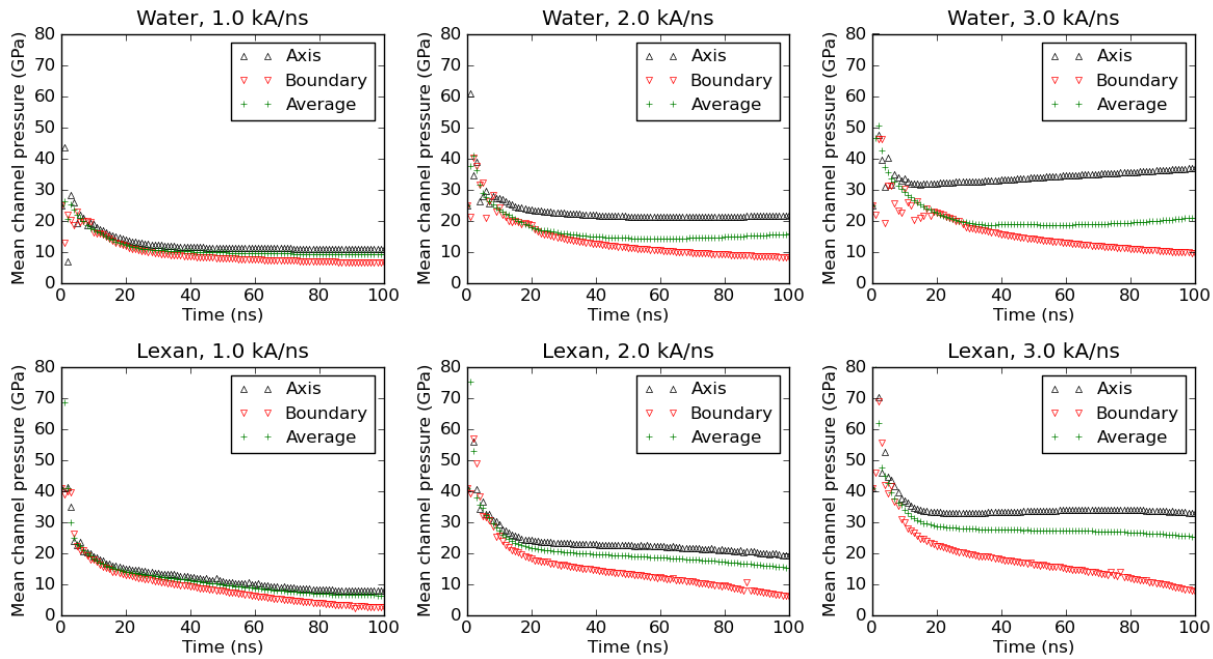

Figure 43: Mean channel pressure histories for water (above) and Lexan (below).

B.5. Channel pressure dependence on ramp rate

Table 8: Average channel pressure in water and Lexan sampled at t = 60 ns for high current ramp rates.

	Pressure (GPa)		
	Water	**Lexan**	**Dense Lexan**
1.0 kA/ns	9.5	8.6	21.8
1.5 kA/ns	12.0	13.8	28.7
2.0 kA/ns	14.2	18.5	34.8
3.0 kA/ns	18.6	27.2	46.1

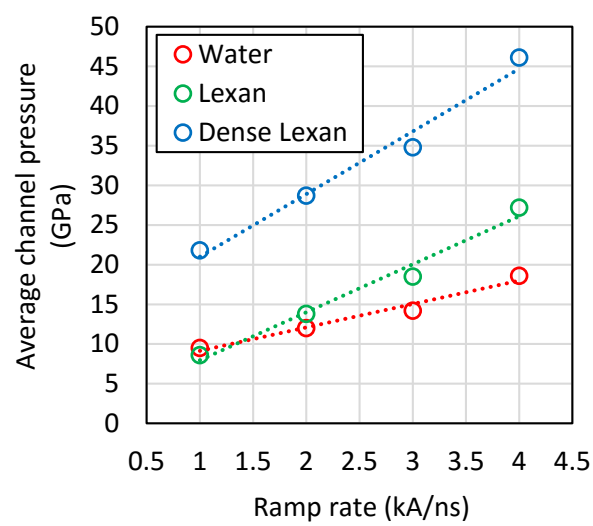

Figure 44: Average channel pressure at t = 60 ns as a function of current ramp rate.

B.6. Mean channel radius histories

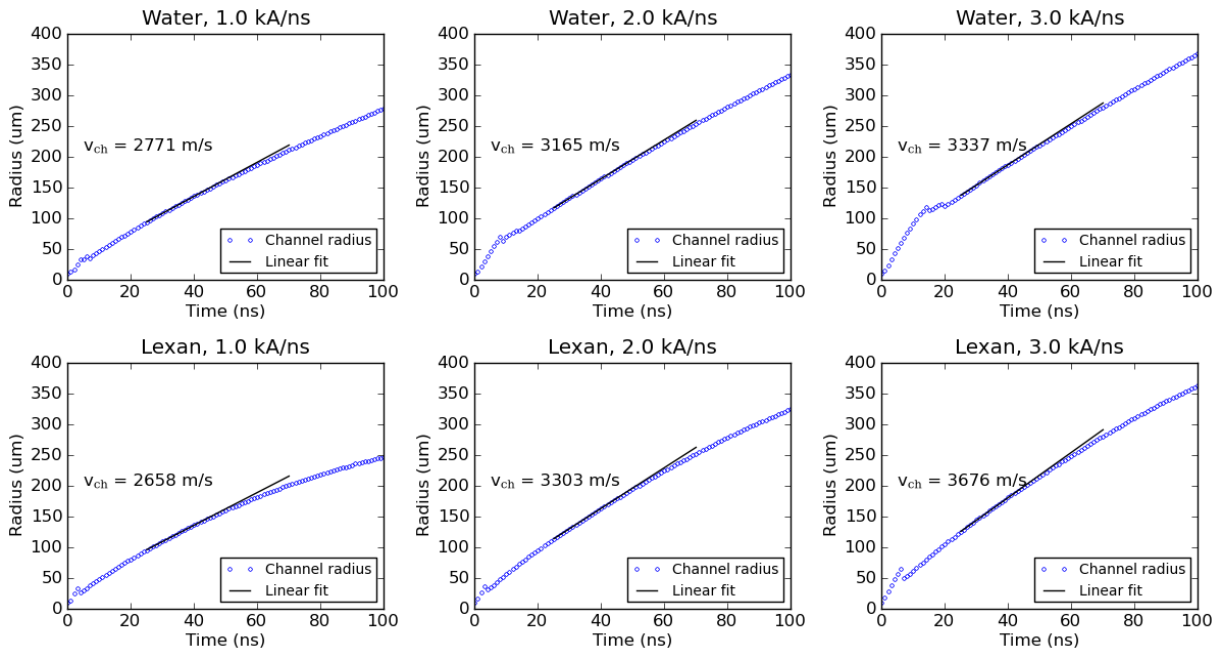

Figure 45: Channel radius histories for water (above) and Lexan (below).

B.7. Coupling coefficient histories

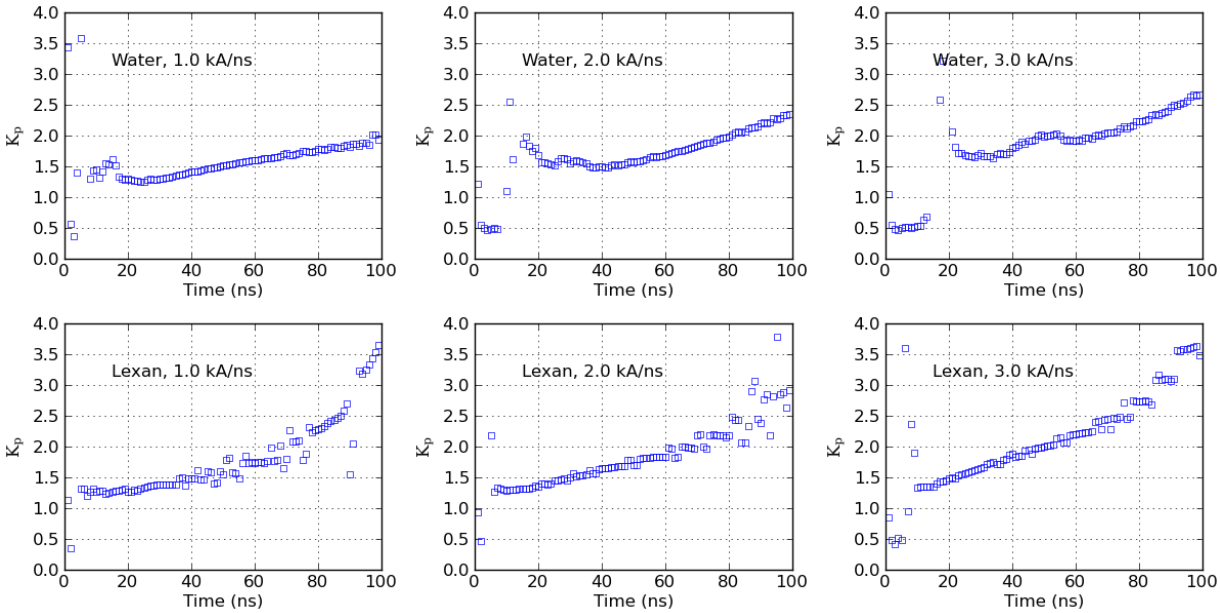

Figure 46: Coupling coefficient (K_p) histories for water (above) and Lexan (below).

APPENDIX C: EXAMPLE INPUT FILE (LEXAN)

```
  title
      Model of Lexan Arc

  Units, SI

$$$$$$$$$$$$$$$$$$$$$$$$$$$$  physics options  $$$$$$$$$$$$$$$$$$$$$$$$$$$$

  radiation magnetohydrodynamics conduction
    cylindrical

    detailed energy tallies

    mesh, inline
      brick
        numx 2
          xblock 1 10.e-6  interval 100
          xblock 2 999.e-6 first size 1.e-7 last size 0.425e-6
        numy 1
          yblock 1 0.5e-6 interval 1
      end
      set assign
        nodeset, ilo, 1
        nodeset, jlo, 2
        nodeset, ihi, 3
        nodeset, jhi, 4
        sideset, ilo, 1
        sideset, jlo, 2
        sideset, ihi, 3
        sideset, jhi, 4
      end
    end

    maximum initial time step = 1.0e-15
    maximum time step limit = 1.0e-11

$ Magnetic specification

    formulation, fife r scaled

    transient magnetics
      void conductivity = 1.0e-6
      rz cyl radial slot bc, sideset 3, function 1, scale 1.0,
           r 0., z 0., -2., -1., 1., 2.
      centerline bc, sideset 1
      aztec set, 1
      current tally 1, sideset 1, sideset 2, sideset 3, sideset 4, end
    end

    function 1
      $ ramprate = {ramprate = RAMP} kA/ns
      0.0   0.0
      1.0   {ramprate*1.e+9*1.e3}  $ convert ns to s and kA to A
    end

    hydrodynamics
      no displacement, sideset 1, r
      no displacement, sideset 3, r
      no displacement, sideset 2, z
      no displacement, sideset 4, z
    end
```

```
    thermal conduction
      no heat flux, sideset 1
      no heat flux, sideset 2
      no heat flux, sideset 4
      scale 1.e30   $ Turn off conduction time step control
      aztec set, 5
    end

    linearized diffusion
      max energy density change = 0.5
      initial conditions, block 1, uniform temperature 11604.5
      initial conditions, block 2, uniform temperature 298.15

      group bounds
        log 0.01 [eV] to 100. [eV] by 1
      end

      reflective boundary, sideset 1
      reflective boundary, sideset 2
      vacuum boundary, sideset 3
      reflective boundary, sideset 4

      outer aztec set, 2
      inner aztec set, 3
      grey  aztec set, 4

    end

    block 1
      lagrangian mesh
      material 1
    end

    block 2
      lagrangian mesh
      material 2
    end


$$$$$$$$$$$$$$$$$$$$$$$$$$$$  user-def var $$$$$$$$$$$$$$$$$$$$$$$$$$$$$$$$

  derived variable, JHEAT
    mesh centering = element
    storage type = scalar
    read variables,
      JE
      SCALAR_CONDUCTIVITY
    end
    "
    double JEMAG2 = JE[0]*JE[0]+JE[1]*JE[1];
    JHEAT[0] = JEMAG2/SCALAR_CONDUCTIVITY[0];
    "
  end

$$$$$$$$$$$$$$$$$$$$$$$$$$$$  tracers  $$$$$$$$$$$$$$$$$$$$$$$$$$$$$$$$

  tracer points
    lagrangian tracer  1   r  9.5e-6  z  0.25e-6
    lagrangian tracer  2   r 10.5e-6  z  0.25e-6
    lagrangian tracer  3   r 12.0e-6  z  0.25e-6
    lagrangian tracer  4   r 20.0e-6  z  0.25e-6
    lagrangian tracer  5   r 60.0e-6  z  0.25e-6
  end
```

```
$$$$$$$$$$$$$$$$$$$$$$$$$$  inline visualization $$$$$$$$$$$$$$$$$$$$$$

  spy

  Image("Density1d",WHITE,BLACK);
    Color(BLACK);
    ULabel("r (m)");
    VLabel("Interior density");
    Window(0,0,1,1);
    FontSize(0.04);
    FontAlignment(LEFT,TOP);
    DrawText(sprintf("Density at t = %.2f ns",1.e9*TIME),0.1,0.99);
    Fix1D(0.,1e-7,1.e-3,1e-7);
    Set1DLineProperties(1.0,1,0xFFFF,BLACK);
    Set1DLineProperties(5,1,SOLID,0,1,0);
    Plot1D("DENSITY+1",ON,ON,"DensityProfile_");
  EndImage;

  endspy

  end    $ End of physics section

$$$$$$$$$$$$$$$$$$$$$$$$$$$  algorithm control  $$$$$$$$$$$$$$$$$$$$$$$$$$$$$$

  aztec 1
   solver, cg
   multilevel
   end
  end

  aztec 2
    solver = gmres
    tol = 1.0e-9
    max iter, 5000
    multilevel
    end
  end

  aztec 3
    solver = cg
    multilevel
    end
  end

  aztec 4
    solver = cg
    multilevel
    end
  end

  aztec 0
     solver,    gmres
     tol,       1.e-12      $ default = 1.e-5
     $max iter,  5000        $ default = 500
     $physics output
     multilevel
     end
   end

   aztec 5
     solver, cg
     conv norm, rhs
   end
```

```
$$$$$$$$$$$$$$$$$$$$$$$$$$$  execution control  $$$$$$$$$$$$$$$$$$$$$$$$$$$$$$

  start time= 0.0
  Termination time = 100.e-9

  Emit plot, time interval=1.0e-9 from 0.0 to 1.0
  Emit hisplt, time interval = 0.1e-9

  Plot variable  $ variables written to exodus file
    coordinates
    velocity
    betheta
    je
    density      : avg
    energy       : avg
    temperature  : avg
    pressure     : avg
    sound speed  : avg
    specific heat vol : avg
    econ         : avg
    econ_par     : avg
    econ_perp    : avg
    thermal_con  : avg, as 'tcon'
    thermal_con_par :  avg
    thermal_con_perp:  avg
    scalar conductivity
    ZBAR         : avg
    OPACITY_A    : avg
    OPACITY_R    : avg
    RAD_ENERGY_DENSITY
    mat_max_coords
    jheat
  end

$$$$$$$$$$$$$$$$$$$$$$$$$$$  material models  $$$$$$$$$$$$$$$$$$$$$$$$$$$$$$$$

  material 1 Lexan
    density = 1185.
    temperature = 11604.5
    model 1
    model 2
    model 3
    number of elements 2  $ Approximate as CH
      element 1, mass 1.00794, fraction 0.5
      element 6, mass 12.011, fraction 0.5
    end
  end

  material 2 Lexan
   density 1185.
   temperature 298.
    model 1
    model 2
    model 3
    number of elements 2  $ Approximate as CH
      element 1, mass 1.00794, fraction 0.5
      element 6, mass 12.011, fraction 0.5
    end
  end

  model 1 keos sesame
    neos = 7751
    feos = 'aneos'
```

```
  end

  model 2 lmd
    material = 'lexan'
  end

  model 3 tabular opacity
    material = 'CH'
  end

$ Water LMD model
$  model 2 lmd
$    z              = 3.3333
$    a              = 6.0053
$    rho solid      = 1.0e3
$    tmelt          = 273.0
$    XIEV           = 14.0
$    G0             = 5.05
$    G1             = 7.95
$    LOG LAMBDA MIN = 2.0
$    P1             = 1.
$    P2a            = 0.2
$    P2b            = 0.0
$    P2c            = 25000.
$    P2d            = 2.0e22
$    P2e            = 2.0
$    P3a            = 0.01
$    P3b            = 0.33
$    P4a            = 1.0
$    P4b            = 0.33
$    P5             = 0.0
$    PRESSURE IONIZATION PREFACTOR = 0.98
$    PRESSURE IONIZATION EXPONENT  = 1.05
$    DIPOLE ALPHA   = 11.5353
$  end

exit
```

DISTRIBUTION

1	MS0492	Kenneth C. Chen	0411
1	MS1152	Roy E. Jorgenson	1352
1	MS1152	Larry K. Warne	1352
1	MS1152	Lori I. Basilio	1352 (electronic copy)
1	MS1321	Glen E. Hansen	1443 (electronic copy)
1	MS1321	Randy M. Summers	1446 (electronic copy)
1	MS1323	John H. J. Niederhaus	1446
1	MS0899	Technical Library	9536 (electronic copy)

Sandia National Laboratories